

A CENSUS OF BARYONS AND DARK MATTER IN AN ISOLATED, MILKY WAY-SIZED ELLIPTICAL GALAXY

PHILIP J. HUMPHREY¹, DAVID A. BUOTE¹, CLAUDE R. CANIZARES², ANDREW C. FABIAN³, JON M. MILLER⁴
Draft version September 26, 2018

ABSTRACT

We present a study of the dark and luminous matter in the isolated elliptical galaxy NGC 720, based on deep X-ray observations made with the *Chandra* and *Suzaku* observatories. The gas properties are reliably measured almost to R_{2500} , allowing us to place good constraints on the enclosed mass and baryon fraction (f_b) within this radius ($M_{2500}=1.6\pm 0.2\times 10^{12}M_\odot$, $f_{b,2500}=0.10\pm 0.01$; systematic errors are typically $\lesssim 20\%$). The data indicate that the hot gas is close to hydrostatic, which is supported by good agreement with a kinematical analysis of the dwarf satellite galaxies. We confirm at high significance ($\sim 20\text{-}\sigma$) the presence of a dark matter (DM) halo. Assuming an NFW DM profile, our physical model for the gas distribution enables us to obtain meaningful constraints at scales larger than R_{2500} , revealing that most of the baryons are in the hot gas. We find that f_b within the virial radius is consistent with the Cosmological value, confirming theoretical predictions that a \sim Milky Way-mass ($M_{\text{vir}}=3.1_{-0.3}^{+0.4}\times 10^{12}M_\odot$) galaxy can sustain a massive, quasi-hydrostatic gas halo. While f_b is higher than the cold (cool gas plus stars) baryon fraction typically measured in similar-mass spiral galaxies, both the gas fraction (f_g) and f_b in NGC 720 are consistent with an extrapolation of the trends with mass seen in massive galaxy groups and clusters. After correcting for f_g , the entropy profile is close to the self-similar prediction of gravitational structure formation simulations, as observed in massive galaxy clusters. Finally, we find a strong heavy metal abundance gradient in the interstellar medium, qualitatively similar to those observed in massive galaxy groups.

Subject headings: dark matter— Xrays: galaxies— galaxies: elliptical and lenticular, cD— galaxies: ISM— galaxies: formation — galaxies: individual (NGC720)

1. INTRODUCTION

In low-redshift disk galaxies of size comparable to the Milky Way, the fraction of cold baryons (cool gas and stars) relative to the total mass is typically found to be significantly less than the cosmological baryon fraction (e.g. Fukugita et al. 1998; McGaugh et al. 2010), which is measured to be 0.17 (Dunkley et al. 2009). This has proven a challenge for standard models of galaxy formation which, in fact, over-predict the observed baryon content by as much as a factor ~ 2 (e.g. Benson et al. 2003). Solutions to this problem, for example strong heating of the interstellar medium (ISM) by active galactic nucleus (AGN) feedback (e.g. Kauffmann et al. 1999) or less efficient cooling (e.g. Maller & Bullock 2004), ultimately involve many of the baryons remaining in a difficult to detect hot phase, which may exist as an extended halo around the galaxy. Models suggest that as many as half the “missing baryons” in the local universe could be in diffuse, pressure-supported halos around normal galaxies (e.g. White & Frenk 1991; Maller & Bullock 2004; Kereš et al. 2005; Fukugita & Peebles 2006; Sommer-Larsen 2006). Such a halo around the Milky Way could help explain the properties of local OVI absorbing clouds (Sembach et al. 2003), the confinement of the Magellanic

stream (Moore & Davis 1994), gas stripping from dwarf satellites (Blitz & Robishaw 2000) and provide a reservoir for the ongoing gas accretion proposed to solve the “G-dwarf problem” (e.g. Sommer-Larsen et al. 2003).

Direct observational evidence for such extended halos around disk galaxies remains controversial. While zero redshift absorption lines in the X-ray spectra of distant quasars clearly indicates diffuse, hot ($\sim 10^6\text{K}$) gas in the vicinity of the Milky Way (e.g. Nicastro et al. 2002; Fang et al. 2002; Rasmussen et al. 2003; Fang et al. 2006; Bregman & Lloyd-Davies 2007; Buote et al. 2009; Fang et al. 2010), the distribution of this gas along the sightline remains unclear (e.g. Yao & Wang 2005; Yao et al. 2008). Other tracers of the putative hot baryons suggest the gas may be confined to the disk (Anderson & Bregman 2010; Henley et al. 2010, although see Joudaki et al. 2010), but the results are highly model-dependent. Attempts to detect gaseous halos around external disk galaxies have, similarly, proven inconclusive. While X-ray emission from diffuse, hot gas associated with star-formation in the disk has been observed (e.g. Fabbiano et al. 2001; Strickland et al. 2004), similar emission from an extended, hot corona has yet to be securely detected (Benson et al. 2000; Rasmussen et al. 2009).

In contrast to disk galaxies, diffuse X-ray emission from massive galaxy groups and clusters has been detected out to scales as large as $\sim R_{1250}\text{--}R_{500}$ ⁵, allowing tight constraints to be placed on the total hot gas content (e.g. Gastaldello et al. 2007b; Sun et al. 2009; Vikhlinin et al.

¹ Department of Physics and Astronomy, University of California at Irvine, 4129 Frederick Reines Hall, Irvine, CA 92697

² Department of Physics and Kavli Institute for Astrophysics and Space Research, Massachusetts Institute of Technology, Cambridge, MA 02139

³ Institute of Astronomy, Madingley Road, Cambridge CB3 0HA, UK

⁴ Department of Astronomy, University of Michigan, Ann Arbor, Michigan 48109

⁵ We define R_Δ as the geometrical radius within which the mean mass density of the system is Δ times the critical density of the Universe.

2006; Allen et al. 2008; Pratt et al. 2009). While the most massive clusters appear to be close to baryonic closure (i.e. the baryon fraction, f_b , at large radii asymptotes to the to the Cosmological value), f_b at lower masses may be significantly smaller (Gastaldello et al. 2007b; Pratt et al. 2009; Giodini et al. 2009; Dai et al. 2009). The gas entropy profiles of groups are systematically enhanced over the predictions of self-similar formation models, suggesting that non-gravitational processes (e.g. feedback during halo assembly) are responsible for ejecting baryons from the central regions of the halo (e.g. Ponman et al. 1999; Pratt et al. 2010; McCarthy et al. 2010). Whether these baryons are completely ejected from the potential well is, however, unclear; extrapolating to R_{vir} , for example, Gastaldello et al. (2007b) found f_b close to the Cosmological value for their group sample.

Giant elliptical galaxies occupy an important niche between Milky-Way sized disk galaxies and galaxy groups, offering a chance to connect these two mass regimes. As the likely end products of spiral galaxy merging, their baryon content may also provide important constraints on how the baryons are distributed in their progenitors. Unlike disk galaxies, *most* of their gas is typically in the form of an extended, hot halo, the X-ray emission from which is often detected out at least to tens of kpc. While early-type galaxies therefore provide an ideal opportunity to take a census of the baryon content in normal galaxies, surprisingly little is known about their f_b . Based on weak lensing studies, the *stellar* mass fraction appears to be small ($\lesssim 0.03$; Hoekstra et al. 2005; Gavazzi et al. 2007), but for massive galaxies, most of the baryons are expected to be in the hot halo (e.g. Kereš et al. 2005). In their hydrostatic X-ray mass analysis of three isolated elliptical galaxies (and four low-mass groups), Humphrey et al. (2006, hereafter H06) were only able to obtain interesting constraints on the total baryon content by employing restrictive priors.

Mathews et al. (2005) showed that the X-ray luminosity (L_X) of the most X-ray bright early-type galaxies is consistent with their being at the centre of massive, baryonically closed groups. However, there is observed to be a huge range of L_X at fixed optical luminosity (Canizares et al. 1987; O’Sullivan et al. 2001; Ellis & O’Sullivan 2006), suggesting that L_X is determined by both the virial mass of the halo in which galaxies lie and their history of feedback (Mathews et al. 2006). In some cases, particularly in the lowest-mass systems, feedback appears to have been strong enough to denude a galaxy largely of its gas (David et al. 2006). Still, it is difficult to map galaxies from the optical *versus* X-ray luminosity plane onto f_b directly, in large part since the gas emissivity depends on the square of its density and gas density profiles are not self-similar (e.g. H06; Gastaldello et al. 2007b; Sun et al. 2009). This means that L_X , which is typically measured within only a small fraction of the virial radius (R_{vir}), is a poor tracer of the overall gas mass. The detailed spatially resolved studies needed to trace the gas distribution to large enough radii to measure f_b more directly have largely been restricted to the most X-ray luminous systems, which tend to lie at the centres of massive groups. Thus, whether early-type galaxies hosted in Milky-Way sized halos can actually maintain a hot halo with a mass comparable to the predictions of disk galaxy formation models remains

an open question.

To begin to address this question, in this paper we present a detailed X-ray study of the isolated elliptical galaxy NGC 720, using deep *Chandra* and *Suzaku* observations (see Table 1). The complementary characteristics of these satellites, i.e. the excellent spatial resolution of *Chandra* (enabling the inner parts of the X-ray halo to be studied in detail) and the low, stable background of *Suzaku* (which is helpful for studying the low surface-brightness outer parts of the halo), make a combination of these data ideal for studying the hot gas properties over as wide a radial range as possible. NGC 720 is a well-studied galaxy with a modest L_X ; for its optical luminosity, it lies roughly in the middle of the scatter in the L_X - L_B relation (O’Sullivan et al. 2001). It has occasionally been labelled a galaxy group (e.g. Garcia 1993; Osmond & Ponman 2004), but within R_{500} the system comprises only one L_* galaxy (NGC 720 itself) and dwarf companions, the brightest of which is three magnitudes fainter than the central galaxy (Dressler et al. 1986; Brough et al. 2006). The total virial mass of the system, derived both from hydrostatic X-ray modelling and from the kinematics of the satellites, is a few times $10^{12}M_\odot$ (H06; Brough et al. 2006), making it only a few times more massive than the Milky Way, and therefore the ideal system for our purposes. Past studies, however, have not provided good constraints on the overall baryon content of the system (H06).

The X-ray emission from the hot gas in NGC 720, which can be traced out to scales of at least ~ 80 kpc (H06), has a relaxed morphology (Buote & Canizares 1994; Buote et al. 2002), suggesting that hydrostatic mass modelling techniques can be reliably used to infer the total gravitating mass (e.g. Buote & Tsai 1995). This is further supported by the lack of significant radio emission (Fabbiano et al. 1987), indicating that there is not currently an AGN that might be stirring up the ISM. For relaxed systems, hydrostatic equilibrium is believed to be an excellent approximation, with non-thermal effects expected to contribute no more than ~ 20 per cent of the total pressure (e.g. Nagai et al. 2007; Piffaretti & Valdarnini 2008; Fang et al. 2009). The overall agreement between the masses inferred from hydrostatic methods and those found by gravitational lensing and stellar dynamical modelling or the predictions of stellar population synthesis models generally support this picture (e.g. Mahdavi et al. 2008; Churazov et al. 2008; Humphrey et al. 2009a). Modest discrepancies have been reported in a few galaxies between hydrostatic X-ray masses and stellar dynamics results (e.g. Romanowsky et al. 2009; Gebhardt & Thomas 2009; Shen & Gebhardt 2010), but these may simply reflect systematic uncertainties in the stellar dynamical modelling (e.g. Gavazzi 2005; Thomas et al. 2007a), or the dynamics of the hot gas at the very smallest scales (Brighenti et al. 2009).

We adopted a nominal distance of 25.7 Mpc for NGC 720, based on the I-band SBF distance modulus estimate of Tonry et al. (2001), which was corrected to account for recent revisions to the Cepheid zero-point (see H06). At this distance, $1''$ corresponds to 123 pc. We assumed a flat cosmology with $H_0 = 70\text{km s}^{-1}$ and $\Omega_\Lambda = 0.7$. We adopted R_{102} as the virial radius (R_{vir}), based on the approximation of Bryan & Norman (1998)

TABLE 1
OBSERVATION SUMMARY

ObsID	Start Date	Exposure (ks)
Chandra		
7062	2006 Oct 9	23
7372	2006 Aug 6	49
8448	2006 Oct 12	8
8449	2006 Oct 12	19
Suzaku		
800009010	2005 Dec 30	177

NOTE. — Details of the observations used in the present analysis. For each dataset we quote the observation identification number (ObsID), the start date and the exposure time, after having removed periods of background “flaring” (Exposure). An additional, shallow *Chandra* observation (ObsID 492) was excluded due to its elevated background level.

for the redshift of NGC 720. Unless otherwise stated, all error-bars represent $1\text{-}\sigma$ confidence limits (which, for our Bayesian analysis, implies the marginalized region of parameter space within which the integrated probability is 68%).

2. DATA ANALYSIS

2.1. *Chandra*

2.1.1. *Data reduction*

The region of sky containing NGC 720 has been imaged by the *Chandra* ACIS instrument in the ACIS-S configuration on 4 separate occasions (a shallow fifth observation was excluded from our analysis due to its enhanced background level), as listed in Table 1. We processed each dataset independently, using the CIAO 4.1 and *Heasoft* 6.8 software suites, in conjunction with the *Chandra* calibration database (*Caldb*) version 4.1.2. To ensure up-to-date calibration, all data were reprocessed from the “level 1” events files, following the standard *Chandra* data-reduction threads⁶. We applied the standard correction to take account of the time-dependent gain-drift and charge transfer inefficiency, as implemented in the *CIAO* tools. To identify periods of enhanced background (which can seriously degrade the signal-to-noise, S/N) we accumulated background lightcurves for each dataset from low surface-brightness regions of the active chips, excluding obvious point-sources. Such periods of background “flaring” were identified by eye and excised. The final exposure times are listed in Table 1. To combine the individual datasets, we merged the final data products (images, spectra, spectral response files, etc.) using the procedure outlined in Humphrey et al. (2008). This involves correcting for relative astrometric errors by matching the positions of detected point sources (allowing for the possibility that some fraction of the sources are transient). Point sources were identified in each observation by applying the *CIAO* `wavdetect` task to the full-resolution 0.5–7.0 keV band image, supplying the exposure-map (computed at an energy of 1.7 keV) to minimize spurious detections at the image boundaries. The detection threshold was set to 10^{-6} , corresponding to $\lesssim 1$ spurious source detections per chip. A final source list was obtained by repeating the source detection procedure on the final, merged image. All detected sources

⁶ <http://cxc.harvard.edu/ciao/threads/index.html>

were confirmed by visual inspection, and, for each, appropriate elliptical regions containing approximately 99% of its photons were generated. We detected 58 point sources within the D_{25} ellipse (de Vaucouleurs et al. 1991), contributing $\sim 20\%$ of the total 0.5–7.0 keV photons in that region.

2.1.2. *Chandra Image*

We examined the image for evidence of morphological disturbances that may complicate deprojection, or possibly suggest perturbation from hydrostatic equilibrium. In Fig 1 we show smoothed, flat-fielded *Chandra* image, having removed the point-sources with the algorithm outlined in Fang et al. (2009). The data were then flat-fielded with the exposure map and smoothed with a Gaussian kernel. Since the S/N of the image varies strongly with off-axis angle, the width of the Gaussian kernel was varied with distance according to an arbitrary power law, ranging from $\sim 1''$ in the centre of the image to $\sim 1'$ at the edge of the field.

The image is smooth and slightly elliptical, showing no clear evidence of disturbances or asymmetries. This is consistent with our findings based on a shallower *Chandra* observation (Buote et al. 2002). To search for more subtle structure in the image, we used dedicated software, built around the MINUIT library⁷, to fit an elliptical beta model (with constant ellipticity) to the central $\sim 2.5'$ wide portion of the unsmoothed image, (correcting for exposure variations with the exposure map)⁸. We show in Fig 1 an indication of deviations from this simple model by plotting $(\text{data-model})^2/\text{model}$, which corresponds to the χ^2 residual in each pixel. To bring out structure, we smoothed this image with a Gaussian kernel of width $1.5''$ (3 pixels). As is clear from this “residuals significance” image, there is no evidence of any coherent residual features. This is unsurprising given the lack of a currently active central black hole, as suggested by the lack a significant radio emission (Fabbiano et al. 1987), nor a central, bright X-ray source.

2.1.3. *Spectral analysis*

We extracted spectra in a series of concentric, contiguous annuli, placed at the X-ray centroid (which was computed iteratively and verified by visual inspection). The widths of the annuli were chosen so as to contain approximately the same number of background-subtracted photons, and ensure there were sufficient photons to perform useful spectral-fitting. The resulting annuli all had widths larger than $\sim 8''$, which is sufficient to prevent the instrumental spatial resolution from producing strong mixing between the spectra in adjacent annuli. The data in the vicinity of any detected point source were excluded, as were the data from the vicinity of chip gaps, where the instrumental response may be uncertain. We extracted products from all the active chips (excluding the S4 CCD, which suffers from considerable noise), making appropriate count-weighted spectral response matrices for each annulus with the standard *CIAO* tasks

⁷ <http://lcgapp.cern.ch/project/cls/work-packages/mathlibs/minuit/index.html>

⁸ We obtained a best-fitting major-axis core radius of $2.6''$, $\beta = 0.38$ and axis ratio of 0.85, consistent with Buote et al. (2002)

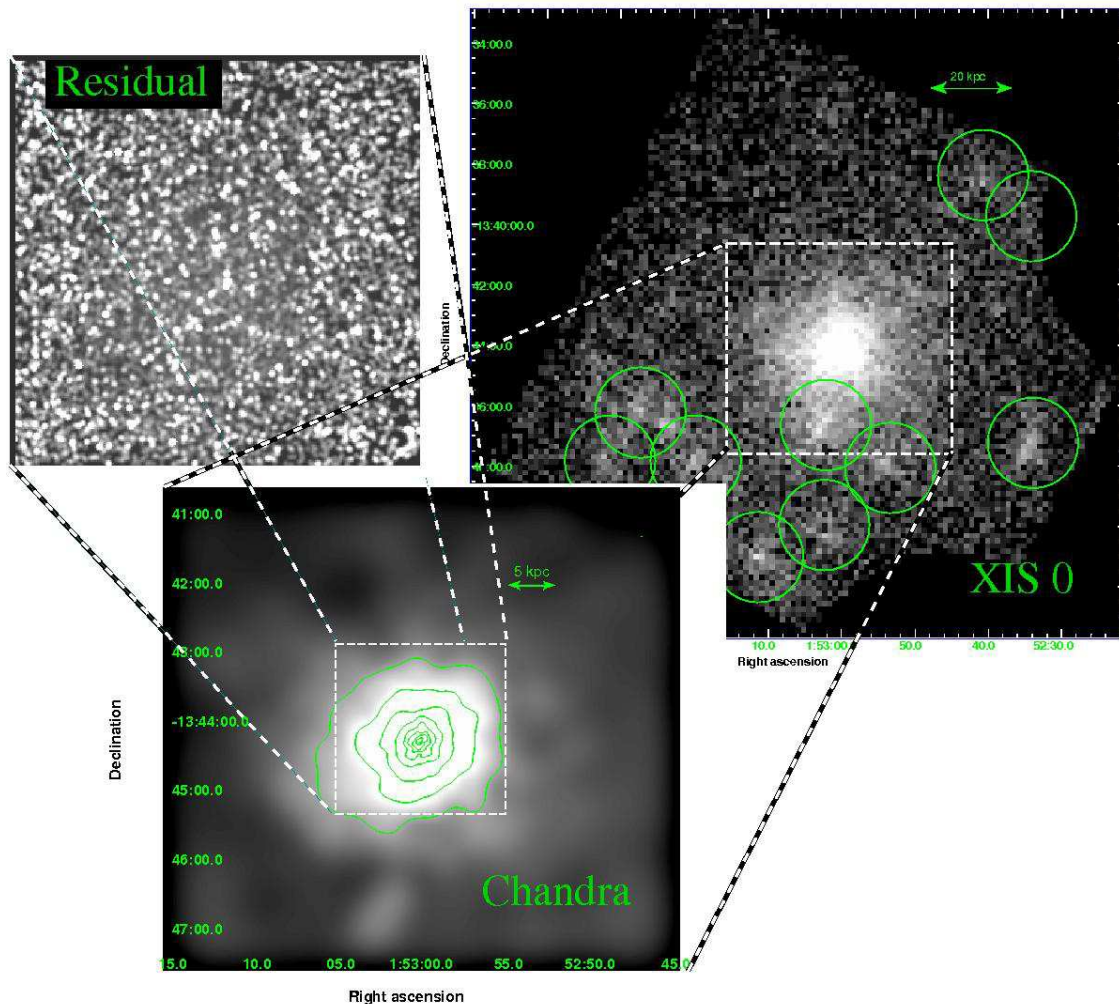


FIG. 1.— *Top right:* *Suzaku* XIS0 image in the 0.5–7.0 keV band, excluding data in the vicinity of the calibration sources. Circular exclusion regions (to mitigate bright point-source contamination) are overlaid. *Bottom:* Smoothed, point-source subtracted *Chandra* X-ray image in the 0.5–7.0 keV band. This image covers only the central part of the ACIS-S3 chip, where the count-rate is sufficiently high for the structure of the X-ray emission to be clearly discerned. The image contrast and smoothing scales were arbitrarily adjusted to bring out key features; the smoothing scale varies from $\sim 1''$ in the central part of the images to $\sim 1'$ in the outer regions. Logarithmically spaced contours are overlaid to guide the eye. *Top left:* “residual significance” image (see text) of the centre of the galaxy, indicating deviations from a smooth model fit to the X-ray isophotes. Although the isophotes are slightly elliptical, the galaxy appears relaxed and symmetric at all accessible scales given its distance.

`mkwarf` and `mkacisrmf`. We extracted identical products individually for each dataset, taking into account the astrometric offsets between them (determined from the image registration discussed above). The spectra were added using the standard *Heasoft* task `mathpha`, and the response matrices were averaged using the *Heasoft* tasks `addrmf` and `addarf`, with weights based on the number of photons in each spectrum. Representative spectra, without background subtraction, are shown in Fig 2, along with the best-fitting source and background models.

Spectral-fitting was carried out in the energy-band 0.5–7.0 keV, using *Xspec* vers. 12.5.1n. We have shown previously that fits to Poisson distributed data which minimize χ^2 can yield significantly biased results, even if we rebin the data to more than the canonical ~ 20 counts per bin (Humphrey et al. 2009b). In contrast, we found that the C-statistic of Cash (1979) typically gives relatively unbiased results. We therefore performed the fits by min-

imizing C, but nonetheless took care to verify there is no significant bias, using the Monte Carlo procedure outlined in Humphrey et al. (2009b). Although not strictly necessary for a fit using the C-statistic, we rebinned the data to ensure a minimum of 20 photons per bin. This aids convergence by emphasizing differences between the model and data. The data in all annuli were fitted simultaneously, to allow us to constrain the source and background components at the same time.

We modelled the source emission in each annulus as coming from a single APEC plasma model with variable abundances, which was modified by Galactic foreground absorption (Dickey & Lockman 1990). Unlike several of our recent studies of galaxies (Humphrey et al. 2006, 2008, 2009a; Humphrey & Buote 2010) we did *not* deproject the data, but instead fitted directly the projected spectra, similar to Gastaldello et al. (2007b). We adopted this procedure since we were interested in ac-

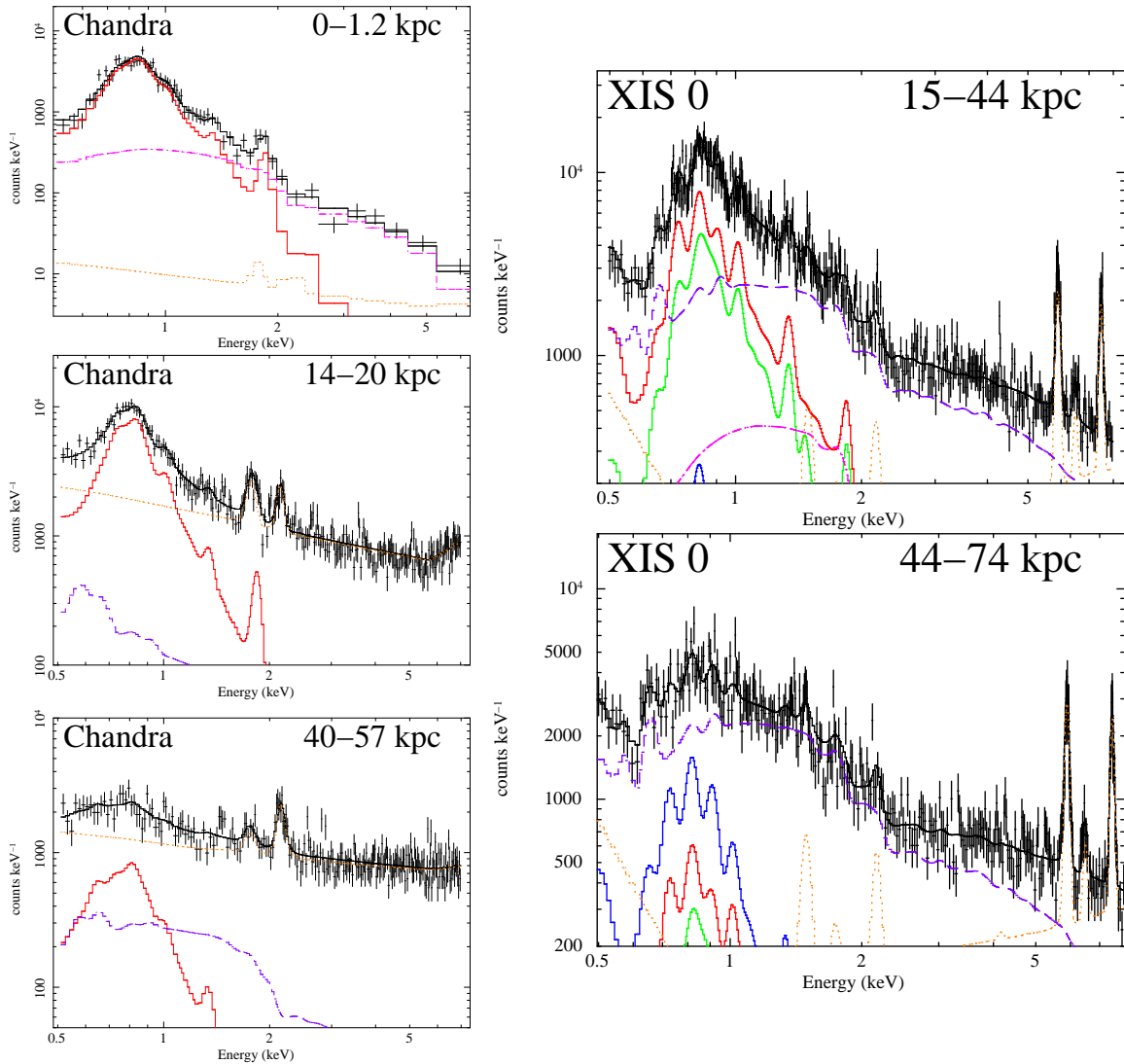


FIG. 2.— Representative *Chandra* and *Suzaku* XIS0 spectra for NGC 720, shown without background subtraction. In addition to the data, we show the best-fitting model, folded through the instrumental response (solid black line), along with the decomposition of this model into its various components. For the *Chandra* data, we show the hot gas contribution (solid red line), the composite emission from X-ray binaries (dash-dot magenta line), the instrumental background (dotted orange) and the cosmic X-ray background (dashed purple line). For the XIS0 data, we show the hot gas emission from each annulus as solid lines (green from the central annulus, red for the second annulus and blue for the third), as well as the X-ray binary component, instrumental background and sky background (using the same colour scheme as for *Chandra*). For *Chandra*, the background is dominated by the instrumental component, whereas for *Suzaku*, which has a lower instrumental background but is less able to resolve the cosmic component into individual point sources, the cosmic component dominates. In all cases, emission from the ~ 0.5 keV gas is detectable above the background below ~ 1 keV.

curately tracing the gas density to the largest available radii; deprojection requires the accurate subtraction of the emission from beyond the outermost radius, which is challenging given the very flat surface brightness profile of this galaxy. In our previous studies, our approximate method for achieving this introduced significant uncertainties into the outermost density data-point, which we have found to be prohibitive here. Since the temperature profile is relatively isothermal, the emission-weighted, projected gas density and temperature can be computed fairly accurately with the “response weighting” algorithm outlined in Appendix B of Gastaldello et al.. We discuss the impact on our results of fitting the deprojected data in § 5.4.

To model the source spectrum, we adopted a slightly modified version of the *Xspec vaepec* model, for which the abundance *ratios* of each species with respect to Fe are

directly constrained. We allowed the abundance of Fe (Z_{Fe}), and the abundance ratios of O, Ne, Mg, Si and Ni with respect to Fe to vary. The other abundances (He) or abundance ratios with respect to Fe (for the other species) were fixed at their Solar values (Asplund et al. 2004). To improve the constraints, Z_{Fe} was tied between multiple annuli, where required, and the abundance ratios were tied between all annuli. The best-fitting abundances (Fig 3), are consistent (in the central part of the system) with previous *Chandra* results from the shallow (17 ks) observation (Humphrey & Buote 2006), and are competitive with those obtained from the very deep *Suzaku* observation (§ 2.2; Tawara et al. 2008), as well as the *XMM* and *Chandra* measurements of the gas in much more massive (and X-ray bright) objects (e.g. Humphrey & Buote 2006; Kim & Fabbiano 2004; Buote et al. 2003). Intriguingly, we note evidence of a significant abundance

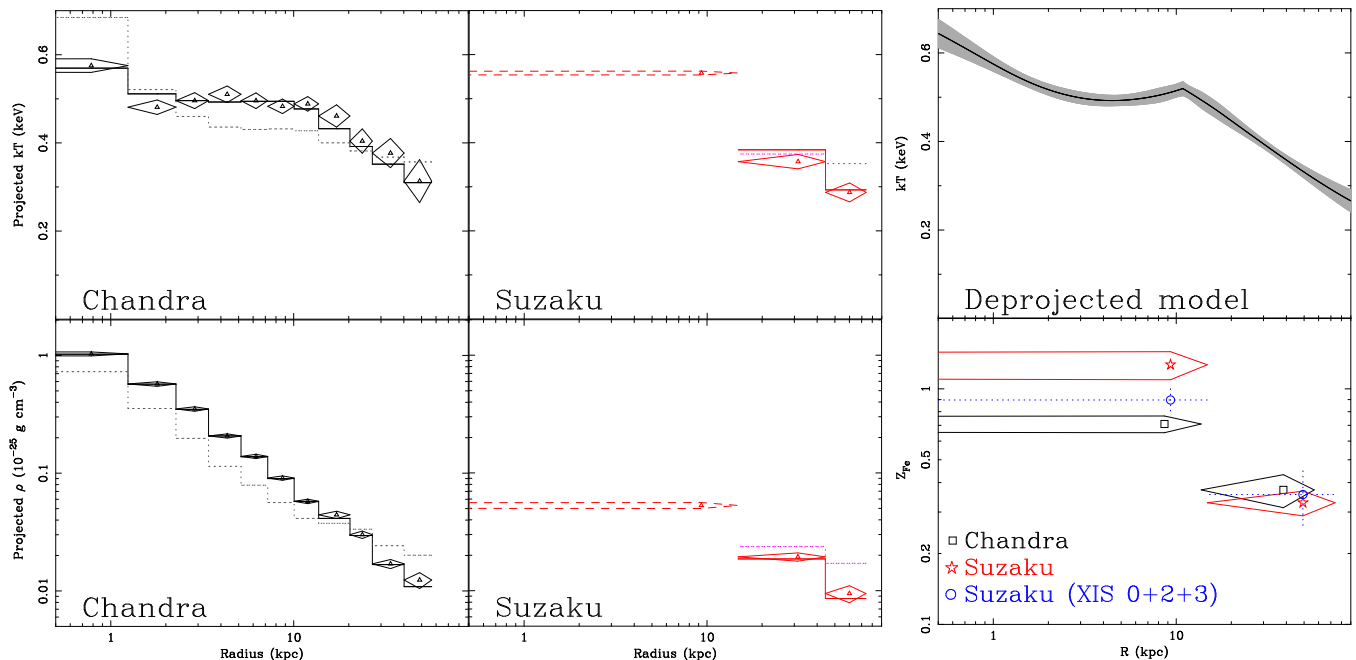


FIG. 3.— Radial projected density, temperature and abundance profiles for NGC 720, obtained with both *Chandra* and *Suzaku*. (For the definition of projected density, see text). Overlaid are the best hydrostatic models for each dataset, which match the data very well. The dotted lines are the best models if dark matter is omitted, for which the fit is very poor. The temperature and density data in the central bin of the *Suzaku* profile were excluded from the fit as the effects of the telescope’s limited spatial resolution are most problematical at this scale, but are shown here as dashed diamonds. The central *Suzaku* abundance data-point appears sensitive to systematic uncertainties (§ 5.8); we show the results for a simultaneous fit of all the XIS units, and for a combination only of units 0, 2 and 3. The displayed error-bars do not take into account any covariance between data-points, which is accounted for in our analysis. In the upper right panel, we show the best-fitting, deprojected temperature profile, and the corresponding $1\text{-}\sigma$ confidence range (shaded region).

gradient in this system (discussed in more detail in § 6.5).

To account for emission from undetected point sources, we included an additional 7.3 keV bremsstrahlung component. Since the number of X-ray point sources is approximately proportional to the stellar light (e.g. Humphrey & Buote 2008), the relative normalization of this component between each annulus was fixed to match the relative K-band luminosity in the matching regions, which we measured from the 2MASS image. To determine the total X-ray binary luminosity, we added the total luminosity of this component, summed over all annuli, to the total L_X of the detected sources within the D_{25} ellipse (de Vaucouleurs et al. 1991)⁹. The resulting L_X , $(2.95 \pm 0.12) \times 10^{40} \text{erg s}^{-1}$, is in excellent agreement with that inferred from extrapolating the point source luminosity function $((2.8 \pm 0.8) \times 10^{40} \text{erg s}^{-1}$; Humphrey & Buote 2008).

To account for the background, we included additional spectral components in our fits, in a variant of the modelling procedure outlined in H06, which were fitted simultaneously to each spectrum, along with the source. To account for the sky background, we included two (unabsorbed) APEC components ($kT=0.07$ keV and 0.2 keV) and an (absorbed) powerlaw component ($\Gamma = 1.41$). The normalization of each component within each annulus was assumed to scale with the extraction area, but the total normalizations were fitted freely. (We discuss the likely impact of the “Solar wind charge exchange” component in § 5.2.1). To account for the instrumental background, we included a number of Gaussian lines and a

broken powerlaw model, which were not folded through the ARF. We included separate instrumental components for the front- and back-illuminated chips, and assumed that the normalization of each component scaled with the area of the extraction annulus which overlapped the appropriate chips. The normalization of each component, and the shape of the instrumental components, were allowed to fit freely. We included two Gaussian lines (at 1.77 and ~ 2.2 keV), the intrinsic widths of which were fixed to zero. The energies of the ~ 2.2 keV lines were allowed to fit freely, as were as the normalizations of all the components.

The best-fitting models are shown in Fig 2 for a representative selection of spectra. To verify the fit had not become trapped in a local minimum, we explored the local parameter space by stepping individual parameters over a range centred around the best-fitting value (analogous to computing error-bars with the algorithm of Cash 1976). Error-bars were computed via the Monte Carlo technique outlined in Humphrey et al. (2006), and we carried out 150 error simulations. In our previous work these simulations were used to generate the standard error on each measured temperature and density data-point, which were assumed to be uncorrelated. In a low-temperature ($\lesssim 1$ keV) system, however, there is a strong degeneracy between the abundance and the gas density. Tying the abundance between multiple annuli, as done in the present work, will consequently result in correlated density errors. Therefore, rather than computing only the error on each data-point from the error simulations, we also computed the covariance between each density data-point, which we fold into our mass modelling (see § 3). (In § 5.8, we show that neglecting

⁹ To obtain L_X for the detected sources, we fitted an absorbed bremsstrahlung model to their composite spectrum.

this effect, or adopting a full treatment that incorporates covariance between all the temperature and density data-points, results in slightly different error-bars and a slight bias, but does not strongly influence our conclusions.) In Fig 3 we show the derived gas temperature, abundance and projected density profiles and the $1\text{-}\sigma$ error-bars on each data-point (assuming the data-points are uncorrelated). The “projected density” is the mean gas density if all the emission measured in the annulus originates from a region defined by the intersection of a cylindrical shell and a spherical shell, both of which have the inner and outer radii as the annulus. Defining it in this way is convenient as it has the units of density, but its precise definition is unimportant, so long as care is taken to compute the models appropriately.

As is clear from Fig 2, the instrumental component dominates the background. This reflects both the strong non X-ray background of the telescope, but also the ability of *Chandra* to mitigate the cosmic component by resolving a significant fraction of it into individual point sources, which were excluded from subsequent analysis. Nevertheless, below ~ 1 keV, the emission from the ~ 0.5 keV gas in NGC 720 dominates at least out to ~ 60 kpc, allowing the gas temperature and density to be constrained. Emission from unresolved point-sources associated with NGC 720 is important only in the innermost few bins, and (as is clear from Fig 2) it can be clearly disentangled from the hot gas component, as it has a very different spectral shape. We note that we have not explicitly included a component to account for the combined emission from cataclysmic variables and hot stars (Revnivtsev et al. 2008). This component, however, is expected to be an order of magnitude fainter than the X-ray binary component, and so this omission will not affect our conclusions (Humphrey et al. 2009a).

2.2. *Suzaku*

The observation of NGC 720 with *Suzaku* was made early in the life of the satellite, while all four XIS units were operating. Data-reduction was performed using the *Heasoft* 6.8 software suite, in conjunction with the XIS calibration database (*Caldb*) version 20090925. To ensure up-to-date calibration, the unscreened data were repipelined with the *aepipeline* task and analysed following the standard data-reduction guidelines¹⁰. Since the data for each instrument were divided into differently telemetered events file formats, we converted the “ 5×5 ” formatted data into “ 3×3 ” format, and merged them with the “ 3×3 ” events files. The lightcurve of each instrument was examined for periods of anomalously high background, but no significant amount of data was found to be contaminated in this way. In Fig 1, we show the 0.5–7.0 keV image for the XIS0 image, excluding data in the vicinity of the calibration sources. A number of off-axis point sources, most likely background AGNs, were identified by visual inspection. To minimize their contamination, we excluded data in a $1.5'$ radius circular region centred on each of these sources. Given the large telescope point-spread function, such a cut will only eliminate $\sim 70\%$ of the photons from these sources. However, we have chosen not to use a larger exclude region, since

it will cut out a large portion of the field of view while only slightly reducing the contamination.

Spectra were extracted in three concentric annuli ($0\text{--}2'$, $2\text{--}6'$ and $6\text{--}10'$), centred at the nominal position of NGC 720 in the field of view of each instrument. Data in the vicinity of the calibration sources and the identified point sources were excluded. For each spectrum, we generated an associated redistribution matrix file (RMF) using the *xismfgen* tool and an estimate of the instrumental background with the *xisnxbgen* task. Since the point-spread function of the telescope is very large ($\sim 2'$ half power diameter), even with such large apertures it is necessary to account for spectral mixing between each annulus. We did this by generating multiple ancillary response files (ARFs) for each spectrum with the *xissimarfgen* tool (Ishisaki et al. 2007), which models the telescope’s optics through ray-tracing. Formally, we wish to model the true spectrum of the hot gas, $T^{gas}(\alpha, \delta, E)$, which is a function of right ascension (α), declination (δ) and energy (E). To make the problem tractable, it is usual practice to adopt an approximation of the form $T^{gas}(\alpha, \delta, E) \simeq \sum_i a_i^{gas}(\alpha, \delta) t_i^{gas}(E) \xi^{gas}(\alpha, \delta)$, where $a_i^{gas}(\alpha, \delta)$ simply delineates discrete, non-overlapping regions of the sky (i.e. $a_i^{gas}(\alpha, \delta) = 1$ if (α, δ) is within region i , or 0 otherwise), and we have assumed that, within region i , the spectrum can be written $t_i^{gas}(E) \xi^{gas}(\alpha, \delta)$, where $t_i^{gas}(E)$ is the normalized spectrum, and ξ^{gas} is the normalization as a function of position on the sky. This is analogous to expanding $T^{gas}(\alpha, \delta, E)$ on a set of basis functions that are separable in E and (α, δ) . For our purposes, each i refers to an annular region on the sky (with outer radii $2'$, $6'$ and $10'$), to correspond to the extraction regions. We approximated ξ^{gas} as a β -model (with parameters chosen to fit the *Chandra* image), correctly normalized to account for the gas emissivity. After passing through the telescope optics, a photon will be detected by the CCDs at some detector coordinate (x, y) and pulse height $(h; \text{corresponding to the energy})$. The pulse height spectrum $P(x, y, h)$ can be written as (e.g. Davis 2001):

$$P(x, y, h) = \int d\alpha d\delta dE K(x, y, h, \alpha, \delta, E) T(\alpha, \delta, E)$$

where K encapsulates the effects of the telescope optics and the instrumental response. Now, we define $D_j(h)$ as the pulse height spectrum accumulated in an extraction region, j , such that $D_j(h) = \int dx dy b_j(x, y) P(x, y, h)$. (Typically we would choose i and j to correspond to the same set of regions on the sky, but that is not essential). Here $b_j(x, y)$ is 1 if (x, y) lies within region j , or 0 otherwise. Thus, we can write:

$$D_j = \sum_i \int dE t_i^{gas} \left[\int dx dy d\alpha d\delta a_i^{gas} b_j \xi^{gas} K \right]$$

Now, we assume that the term in square brackets can be replaced by a product of two new terms, $R_j(E, h)$ and $A_{ij}^{gas}(E)$. With this definition, these new terms correspond, respectively, to the redistribution matrix and ancillary response matrix that can be created with the tasks *xismfgen* and *xissimarfgen*. Hence,

$$D_j(h) = \sum_i \int dE t_i^{gas}(E) R_j(E, h) A_{ij}^{gas}(E) \quad (1)$$

¹⁰ <http://heasarc.gsfc.nasa.gov/docs/suzaku/analysis/abc/>

Spectral fitting involves adopting a parameterized form for the spectrum $t_i(E)$ and comparing the corresponding model $D_j(h)$ to the observed pulse-height spectrum. Unlike *Chandra*, for which the mixing between annuli was negligible (so that $A_{ij}^{gas}(E) = 0$ if $i \neq j$), it was necessary to include all the ARFs A_{ij}^{gas} in the *Suzaku* fitting, which can be done with *Xspec*. The spectra from all extraction regions j were fitted simultaneously, to allow all three $t_i(E)$ models to be constrained. We note that the *Xspec suzpsf* model can be used to perform a more approximate correction for the mixing between annuli. However, our approach more formally accounts for the spatial distribution of the source photons, and is more practical for our present purposes. The spectra from all instruments were fitted simultaneously, allowing additional multiplicative constants in the fit to enable the relative normalization of the model for each instrument to vary with respect to the XIS 0.

It is necessary to add additional components to account for unresolved LMXBs and for the background components. The ARF terms ($A_{ij}(E)$) depend not only on the extraction region geometry but also the spatial distribution of the source photons, which clearly differs between the gas, LMXB and background components. Therefore, it is necessary to generate additional ARFs for each component. For each of these new components, we assume that the spectral shape does not vary with α and δ , and so we can write $T^{lmb}(E) = \xi^{lmb}(\alpha, \delta) t^{lmb}(E)$, and similar terms for the background. We adopt a 7.3 keV bremsstrahlung model for $t^{lmb}(E)$, and allow its normalization to be fitted freely. Since LMXBs should trace the stellar light, we used the K-band 2MASS image (appropriately normalized) to define the term ξ^{lmb} . Folding all of the components into the fitting, eqn 1 is modified to:

$$\begin{aligned}
 D_j(h) = & \sum_i \int dE t_i^{gas}(E) R_j(E, h) A_{ij}^{gas}(E) \\
 & + \int dE t^{lmb}(E) R_j(E, h) A_j^{lmb}(E) \\
 & + \int dE t^{sky}(E) R_j(E, h) A_j^{sky}(E) \\
 & + \int dE t^{inst}(E) \bar{R}_j(E, h) \quad (2)
 \end{aligned}$$

Here we consider separately the sky and instrumental (“inst”) background contributions. For the former, we adopted two APEC plasma models plus a powerlaw term, as described in § 2.1.3, and assume that its surface brightness does not vary over the field of view when computing $A_j^{sky}(E)$. For the latter term, we adopted two, complementary, approaches. One is to subtract off the spectrum generated for each annulus by *xisnxbgen*, in which case the last term in Eqn 2 will be omitted. The other method, which we adopted by default as it provides greater generality in our fits, is to model the instrumental background, similarly to the treatment of this component with *Chandra*. We found that a single broken power law, plus Gaussian lines (at $\sim 1.5, 1.7, 2.2, 5.9, 6.5$ and 7.5 keV), was sufficient for our purposes here, provided the model was not multiplied by the effective area curve. Unfortunately, the quantum efficiency is folded

into the RMF created by *xisrmfgen*, and so we first had to normalize the RMF through which this model was folded (the “renormalized” response matrix being indicated by \bar{R}_j in eqn 2). Still, we found that the precise shape of the instrumental term is not important since it is a relatively minor component in the spectral model (except in the vicinity of the calibration lines). We did not obtain significantly different results if we used the modelling method or the direct subtraction method for the instrumental contribution (§ 5.2).

We found that our model was able to capture the shape of the spectra well. The best-fitting normalization of the LMXB component corresponds to an LMXB luminosity of $(3.08 \pm 0.07) \times 10^{40} \text{ erg s}^{-1}$, in excellent agreement with the *Chandra* data, and with the extrapolation of the detected LMXB luminosity function. Representative spectra are shown in Fig 2, showing the various model components. It is immediately clear that the spectral mixing between annuli is significant. For example, $\sim 20\%$ of the photons from the central bin are scattered into the second annulus. *Failure to take account of this effect actually results in a significantly different temperature profile, which is almost isothermal at ~ 0.5 keV, and very inconsistent with the Chandra data.* The background is dominated by the sky component, which is more significant than in *Chandra* since very few of the point sources that dominate it above ~ 1 keV can be resolved and excluded.

The hot gas temperature, abundance and projected density profiles are shown in Fig 3. In the two outer annuli, the data are in good agreement with the results from *Chandra*. In the innermost annulus, however, we found some discrepancies. Specifically, the abundance is significantly higher than observed with *Chandra*, while the temperature is slightly higher than an emission-weighted average of the *Chandra* temperature profile in this region. The *Suzaku* results in the central bin are, however, sensitive to systematic uncertainties in our modelling procedure (see § 5). In particular, if we omitted data from the XIS1 unit from our fits, we obtained Z_{Fe} in much better agreement with *Chandra* (Fig 3). While this may point to problems with the calibration of the XIS1 unit, it may also be related to errors in the correction we applied to account for spectral mixing between the different annuli. If we omit this correction, for example, the discrepancy with *Chandra* is significantly reduced ($Z_{\text{Fe}} \sim 0.9$). The real temperature profile is clearly more complex than we assume when performing this correction, which may be partially responsible, as there may be slight errors in the ray-tracing algorithm. Furthermore, the single-temperature model fitted to the large *Suzaku* regions, within which the *Chandra* data reveal temperature gradients, would not be expected to yield perfectly consistent results with the *Chandra* data. In any case, we omit the data from the central *Suzaku* annulus in our subsequent modelling, since the *Chandra* data are expected to be more reliable on these scales.

3. MASS MODELLING

We translated the density and temperature profiles into mass constraints using the entropy-based “forward-fitting” technique outlined in H08 and Humphrey et al. (2009a). Briefly, given parametrized profiles of “entropy”

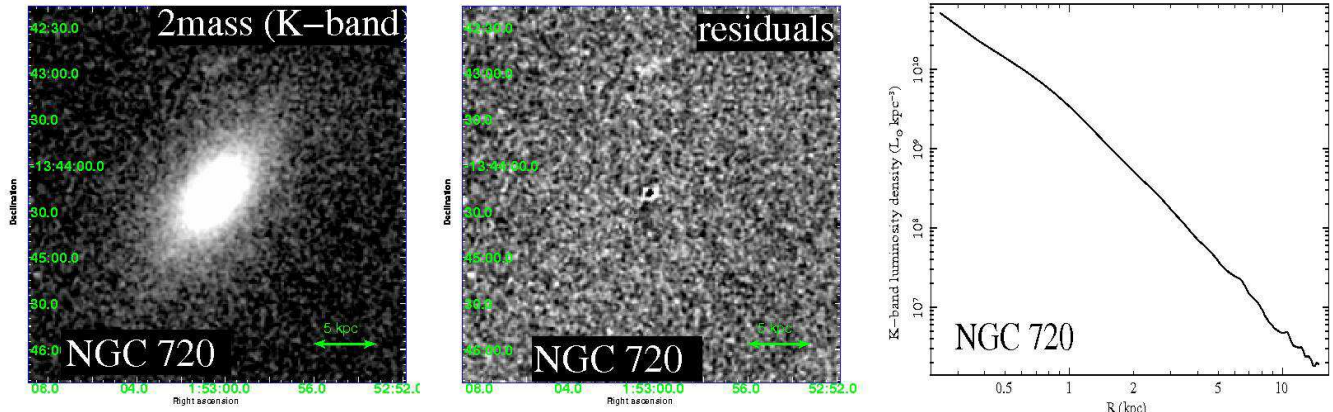


FIG. 4.— *Left*: K-band 2MASS image of NGC 720. *Centre*: residual image, having subtracted our projected model for the three-dimensional light distribution. Overall, this model provides a good fit to the stellar light distribution. A small, coherent residual feature is visible towards the top of the image, which may not be associated with the galaxy. If it is a part of NGC 720, its luminosity is too faint to affect our conclusions. *Right*: the spherically averaged mass density as a function of 3-dimensional radius from our model.

($S = kTn_e^{-2/3}$, where n_e is the electron density) and gravitating mass (excluding the gas mass, which is computed self-consistently), plus the gas density at some canonical radius (for which we used 10 kpc), the three-dimensional temperature and density profiles can be calculated, under the hydrostatic equilibrium approximation and fitted to the data. This model assumes spherical symmetry, which is a standard assumption in X-ray hydrostatic modelling, even when the X-ray isophotes are not perfectly round, since deviations from sphericity are expected to contribute only a relatively small error into the recovered mass profile (e.g. Piffaretti et al. 2003; Gavazzi 2005), and the inferred baryon fraction (Buote & Humphrey 2010).

For the gravitating mass model (in addition to the gas mass), we explored two possible models. Firstly, we considered a model without dark matter, so that the gravitating mass comprised only a stellar component, a supermassive black hole (with mass fixed at $3 \times 10^8 M_{\odot}$, which is that estimated from the $M_{\text{BH}} - \sigma_*$ relation of Tremaine et al. 2002, given the central velocity dispersion value listed in the HyperLEDA database), and the mass of the gas. We assumed the stellar mass component followed the optical light, but allowed the mass-to-light (M/L) ratio to be fitted freely. In the second model, we also included an NFW (Navarro et al. 1997) dark matter halo, the virial mass and concentration (defined as the ratio of the virial radius to the characteristic scale of the NFW model) of which were allowed to fit freely. To model the stellar light, we deprojected the K-band 2MASS image using the method outlined in Humphrey et al. (2009a), which is based on the algorithm of Binney et al. (1990). This entailed first fitting an arbitrary, analytical model to the 2MASS image, which was deprojected analytically onto an arbitrary axisymmetric grid, for a given inclination angle. Since NGC 720 exhibits a very elliptical optical morphology, it is improbable that it is being observed at a low (face-on) inclination angle, and so we initially assumed a 90° inclination (but investigate the effect of using lower inclinations in § 5.6). A series of Lucy (1974) relaxation iterations gradually improved the deprojection. In Humphrey et al. (2009a), we demonstrated that this algorithm gives results consistent with the alternative deprojection technique of Gebhardt

et al. (1996). Since the innermost region within which we extracted the *Chandra* data has a radius of $\sim 10''$, it was not necessary to deconvolve the seeing from the 2MASS image prior to deprojection. We show in Fig 4 the K-band 2MASS image, the residuals from the projection of our axisymmetric model (demonstrating the excellent fit), and the spherically averaged stellar light density profile. Although this method yields an axisymmetric three-dimensional light profile, following Humphrey et al. (2009a), we subsequently averaged it spherically for use with our X-ray modelling (see Buote & Humphrey 2010).

To fit the three-dimensional entropy profile we assumed a model comprising a broken powerlaw, plus a constant; such a model is reasonably successful at reproducing the entropy profiles of galaxies and galaxy groups over a wide radial range (Humphrey et al. 2009a; Jetha et al. 2007; Finoguenov et al. 2007; Gastaldello et al. 2007a; Sun et al. 2009). The normalization of the powerlaw and constant components, the radius of the break and the slopes above and below it were allowed to fit freely. We investigate the impact of varying the slope outside the range of the data (~ 80 kpc) between reasonable limits, which should bound all plausible extrapolated entropy profiles, in § 5.3.

Following Humphrey et al. (2008), we solved the equation of hydrostatic equilibrium to determine the gas properties as a function of radius, from 10 pc to a large radius outside the field of view. For the latter, we adopted the virial radius of the system defined by ignoring the baryonic components (which is slightly smaller than the true virial radius of the system)¹¹. For any arbitrary set of mass and entropy model parameters, it is not always possible to find a physical solution to this equation over the full radial range. Such models were therefore rejected as unphysical during parameter space exploration. In order to compare to the observed *projected* density and temperature profiles, we projected the three-dimensional gas density and temperature, using a procedure similar to

¹¹ For the constant M/L ratio model, we found it more convenient to use a less conservative, smaller radius. Specifically we used 75 kpc, and found the model agreed even less well if a larger scale was adopted.

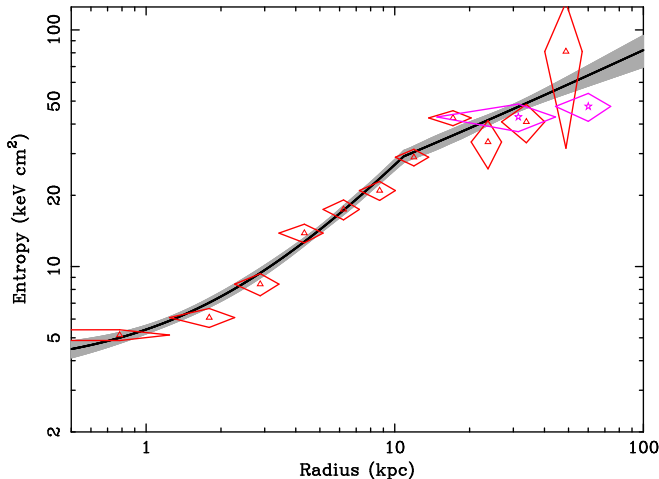


FIG. 5.— Best-fitting entropy profile from fitting the projected data (solid line). The grey shaded region indicates the approximate 1- σ scatter. The sharpness of the break at ~ 14 kpc is a consequence of the simple, broken powerlaw parameterization we adopted for the entropy profile. Overlaid are data-points obtained directly from the deprojected *Chandra* (triangles) and *Suzaku* (stars) data (§ 5.4), which agree well with the projected fit. The deprojected data points have much larger errors as deprojection tends to amplify noise, and the model fit uses both *Chandra* and *Suzaku* data.

that described in Gastaldello et al. (2007b)¹². This involves computing an emission-weighted projected mean temperature and density in each radial bin, that can be compared directly to the data¹³.

To compare the model to the data, we used the χ^2 statistic, fitting simultaneously the *Chandra* and *Suzaku* temperature and density profiles, with the central bin of the *Suzaku* data excluded from our fits. Correlations between the density errors were simply implemented by adopting a form for the χ^2 statistic which incorporates the covariance matrix (e.g. Gould 2003)¹⁴. The probability density function (of the data, given the model) is modified in a similar manner when folding in the non-diagonal elements of the covariance matrix. Parameter space was explored with a Bayesian Monte Carlo method. Specifically, we used version 2.7 of the MultiNest code¹⁵ (Feroz & Hobson 2008; Feroz et al. 2009). Since the choice of priors is nontrivial, we followed convention in cycling through a selection of different priors and assessing their impact on our results (we discuss this in detail in § 5.5). Initially, however, we adopted flat priors on the logarithm of the dark matter mass (over the range $10^{12} < M < 10^{16} M_{\odot}$), the logarithm of the dark matter halo concentration, c_{DM} (over the range $1 < c_{DM} < 100$), the logarithm of the gas density at the

¹² In computing the plasma emissivity term, we approximated the true three dimensional abundance profile with the projected abundance profile (Fig 3); since the profile is relatively flat, this should be sufficient for our present purposes.

¹³ We note that, for systems with a strong temperature gradient and $kT \gtrsim 3$ keV the emission-weighted temperature may be biased low (Mazzotta et al. 2004). For the temperature of NGC 720 the effect is expected to be weak (Buote 2000), which we confirm given the lack of any significant bias we find when fitting the deprojected data, rather than the projected data (§ 5.4).

¹⁴ By default we only consider correlations between the density data, but we investigate introducing a more complete covariance computation in § 5.8 and find that the results are not significantly affected.

¹⁵ <http://www.mrao.cam.ac.uk/software/multinest/>

TABLE 2
ENTROPY AND PRESSURE FIT RESULTS

Parameter	Marginalized value	Best-fit	units
$\log_{10} \rho_{g,10}$	-26.27 ± 0.02	(-26.28)	[g cm^{-3}]
S_c	3.9 ± 0.6	(3.7)	keV cm^2
S_0	23 ± 2	(23)	keV cm^2
β_1	1.14 ± 0.19	(1.13)	
R_{brk}	$11.6^{+3.0}_{-2.4}$	(10.9)	kpc
β_2	0.47 ± 0.13	(0.51)	

NOTE. — Marginalized value and 1- σ errors on the deprojected gas density at 10 kpc ($\rho_{g,10}$), and the entropy parameters. The fitted entropy model within 100 kpc has the form $S(R) = S_c + S_0 f(R)$, where $f(R) = R_{10}^{\beta_1}$, if $R < R_{brk}$, or else $f(R) = (R_{brk}/10 \text{ kpc})^{\beta_1 - \beta_2} R_{10}^{\beta_2}$, and $R_{10} = R/10 \text{ kpc}$. Since the best-fitting set of parameters need not be identical to the marginalized values, we also list the best-fitting value for each parameter.

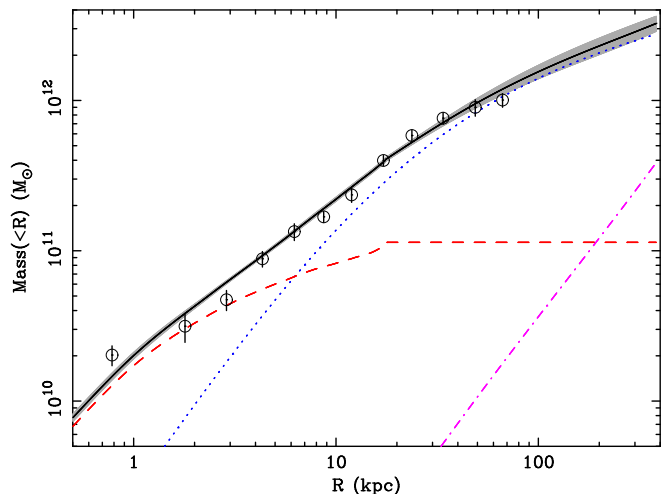


FIG. 6.— Radial mass profile of NGC 720. The solid (black) line indicates the total enclosed mass, the dashed (red) line indicates the stellar mass, the dotted (blue) line is the dark matter contribution and the dash-dot (magenta) line is the gas mass contribution. The grey shaded regions indicate the 1- σ error on the total mass distribution. Overlaid are a set of data-points derived from the more “traditional” mass analysis of this system described in Humphrey & Buote (2010), which generally agrees very well with the fitted model (we stress the model is *not* fitted to these data-points, but is derived separately). Note that the kink in the stellar mass model at ~ 20 kpc is an artefact of the stellar light deprojection technique, but does not affect our results (§ 5.6).

canonical radius, the stellar M/L_K ratio, and the various entropy parameters. For a more detailed description of the modelling procedure, see Humphrey et al. (2008, 2009a).

4. RESULTS

4.1. No dark matter model

We first consider the case without a dark matter halo component. Although our previous work (e.g. H06) has found that the M/L ratio rises steeply with radius (implying that dark matter is needed at high significance), given the high-quality data in NGC 720, it is of particular interest to quantify how poorly the constant M/L ratio model fits these data. We find that the best-fitting model without dark matter is a very poor description of the temperature and density profiles (Fig 3; $\chi^2/\text{dof}=413/19$, with a mean absolute fractional devia-

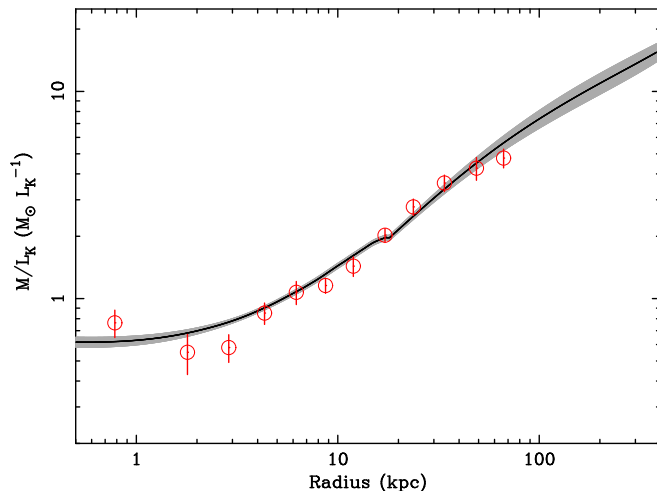


FIG. 7.— Radial total mass-to-K-band light profile of NGC 720. The shaded region indicates the $1\text{-}\sigma$ scatter about the best-fitting relation. The steep rise with radius outside $\sim R_e$ indicates the presence of a massive DM halo. The small kink in the profile around ~ 20 kpc is an artefact of the stellar light deprojection technique, and is unrelated to the break in the entropy profile at ~ 10 kpc. Overlaid are a series of data-points derived from the more traditional mass analysis shown in Fig 6. We stress that the data-points are derived independently and the model is *not* fitted to these data.

tion between the data and models of $\sim 29\%$). As found by Buote et al. (2002), based on an analysis of the X-ray image in NGC 720, the stellar mass component is too centrally concentrated to produce the observed gas pressure profile.

4.2. Dark matter halo

As is clear in Fig 3, when a dark matter halo component was added, the hydrostatic model was able to capture the overall shape of the projected density and temperature profiles very well ($\chi^2/\text{dof}=12.7/17$). The improvement to the fit when dark matter was included was therefore highly significant; the ratio of the Bayesian “evidence” returned by the fitting algorithm (see Feroz & Hobson 2008) for the two cases is 10^{-85} , implying that dark matter is required¹⁶ at $\sim 19.6\text{-}\sigma$.

In Fig 5 we show the best-fitting entropy profile (and its $1\text{-}\sigma$ confidence range), which shows a flattening at large radius similar to two of the three galaxies studied in Humphrey et al. (2009a). As we will show later (§ 6.4), the entropy profile shape, even when extrapolated to large radius, is consistent with trends seen in galaxy clusters (Pratt et al. 2010). The derived radial distribution of the gravitating mass is shown in Fig 6 and the total mass-to-light ratio is shown in Fig 7. In Fig 6 we also show the contribution to the mass from each separate component. We find that the stars dominate the mass distribution within the central ~ 5 kpc, but a significant dark matter halo is required to reproduce the data at larger radii, consistent with our previous study of this system, using data from a much shallower observation

¹⁶ Although not correct in this case (Protassov et al. 2002), for reference, it is interesting to quote the significance of the dark matter detection in frequentist terms by using the F-test; in this case, such an improvement in χ^2 would occur by random chance with a probability of 1.4×10^{-13} , implying a $\sim 7.4\text{-}\sigma$ detection of dark matter.

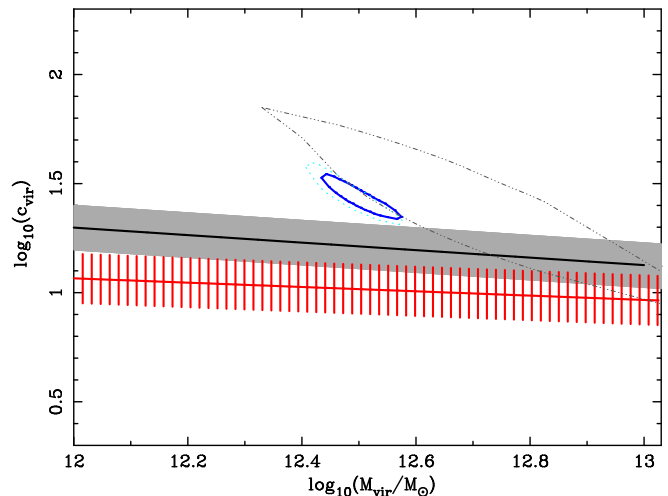


FIG. 8.— Inferred $c_{\text{vir}}\text{-}M_{\text{vir}}$ relation for NGC 720. We show the marginalized $1\text{-}\sigma$ joint confidence region for c_{vir} and M_{vir} based on our fits (solid blue line). The dotted (light blue) curve is the same but for the deprojected data (§ 5.4), and the dot-dash-dash region is the $1\text{-}\sigma$ error region found by H06. The solid black line and grey shaded region are the mean $c_{\text{vir}}\text{-}M_{\text{vir}}$ relation, and $1\text{-}\sigma$ scatter found by Buote et al. (2007), and the red shaded region is the theoretical relation for relaxed halos from Macciò et al. (2008).

(Humphrey et al. 2006). The hot gas becomes the dominant baryonic component outside ~ 200 kpc ($\sim R_{500}$). Overlaid are a series of mass data-points derived from fitting the *deprojected Chandra* data using a more traditional (but more uncertain) mass-modelling method (for more details see § 5.4 and Humphrey et al. 2009a), which agree well with the inferred mass distribution, indicating that the resulting mass profile is not overly sensitive to the analysis method.

A notable feature of the recovered mass distribution is its flattening outside ~ 20 kpc, which allows us to constrain the scale radius, and hence the virial mass of the dark matter halo. In Fig 8, we show the relation between the concentration of the gravitating mass, c_{vir} , and the virial mass, M_{vir} . To be consistent with our past work (Buote et al. 2007), the M_{vir} and R_{vir} are derived from the distribution of the *total* gravitating mass, not just the dark matter, and the *total* concentration, c_{vir} is defined as the ratio of R_{vir} to the characteristic scale of the DM halo. These results are consistent with those obtained by H06 with *Chandra*, but the constraints are very much tighter, reflecting both the significantly deeper observation (~ 5 times deeper *Chandra* observation, combined with the data from the very deep *Suzaku* observation) as well as improvements in our mass modelling procedure. Overlaid on Fig 8 we show the theoretical concentration *versus* mass relation from dark matter only simulations (Macciò et al. 2008, adopting their “ ΛCDM1 ” relation for relaxed halos), and the empirical relation from Buote et al. (2007). NGC 720 lies above both relations, but is within the $2\text{-}\sigma$ scatter obtained by Buote et al.. The best-fitting marginalized model parameter values and confidence regions are given in Tables 2 and 3.

In contrast to our measurement in Humphrey et al. (2006), our adopted modelling procedure did *not* require us to adopt a strong prior on f_b in order to obtain interesting virial mass constraints. This allows us to measure f_b directly from our fit. In Fig 9, we show how the enclosed baryon fraction and gas fraction vary as a function

TABLE 3
MASS RESULTS AND ERROR BUDGET

Test	M_*/L_K $M_\odot L_\odot^{-1}$	$\log M_{2500}$ [M_\odot]	$\log c_{2500}$	$\log M_{500}$ [M_\odot]	$\log c_{500}$	$\log M_{\text{vir}}$ [M_\odot]	$\log c_{\text{vir}}$
Marginalized	$0.54^{+0.03}_{-0.05}$	$12.18^{+0.06}_{-0.05}$	0.86 ± 0.08	$12.34^{+0.07}_{-0.05}$	1.15 ± 0.07	$12.49^{+0.06}_{-0.04}$	1.43 ± 0.08
Best-fit	(0.54)	(12.20)	(0.85)	(12.36)	(1.14)	(12.51)	(1.42)
Systematic error estimates							
ΔDM	$+0.07 \left(\begin{smallmatrix} +0.03 \\ -0.05 \end{smallmatrix} \right)$	$+0.12 (\pm 0.03)$	$+0.46 (\pm 0.08)$	$+0.30 (\pm 0.03)$	$+0.52 (\pm 0.08)$	$+0.48 (\pm 0.03)$	$+0.58 (\pm 0.08)$
ΔAC	$-0.165 (\pm 0.04)$	$+0.03 (\pm 0.06)$	$-0.092 (\pm 0.09)$	$+0.05 (\pm 0.07)$	$-0.087 (\pm 0.09)$	$+0.05 (\pm 0.06)$	$-0.089 (\pm 0.09)$
$\Delta\text{Background}$	$-0.077 (\pm 0.05)$	$-0.051 (\pm 0.04)$	$+0.11 \left(\begin{smallmatrix} +0.07 \\ -0.08 \end{smallmatrix} \right)$	$-0.059 (\pm 0.05)$	$+0.10 (\pm 0.07)$	$-0.059 \left(\begin{smallmatrix} +0.05 \\ -0.04 \end{smallmatrix} \right)$	$+0.10 (\pm 0.07)$
ΔSWCX	$-0.057 (\pm 0.05)$	$-0.059 \left(\begin{smallmatrix} +0.05 \\ -0.03 \end{smallmatrix} \right)$	$+0.10 (\pm 0.08)$	$-0.055 (\pm 0.05)$	$+0.10 \left(\begin{smallmatrix} +0.07 \\ -0.08 \end{smallmatrix} \right)$	$-0.078 \left(\begin{smallmatrix} +0.05 \\ -0.03 \end{smallmatrix} \right)$	$+0.10 (\pm 0.08)$
$\Delta\text{Entropy}$	$-0.014 (\pm 0.04)$	$+0.005 (\pm 0.06)$	$\pm 0.01 (\pm 0.08)$	$+0.008 (\pm 0.07)$	$+0.01 (\pm 0.08)$	$-0.033 \left(\begin{smallmatrix} +0.09 \\ -0.06 \end{smallmatrix} \right)$	$+0.02 (\pm 0.09)$
Δ3d	$-0.008 (\pm 0.05)$	$-0.016 (\pm 0.07)$	$+0.009 (\pm 0.10)$	$-0.031 \left(\begin{smallmatrix} +0.10 \\ -0.06 \end{smallmatrix} \right)$	$+0.01 (\pm 0.10)$	$-0.031 \left(\begin{smallmatrix} +0.08 \\ -0.04 \end{smallmatrix} \right)$	$+0.02 \left(\begin{smallmatrix} +0.09 \\ -0.12 \end{smallmatrix} \right)$
$\Delta\text{Spectral}$	$\pm 0.04 (\pm 0.06)$	$+0.17 \left(\begin{smallmatrix} +0.08 \\ -0.06 \end{smallmatrix} \right)$	$+0.05 (\pm 0.09)$	$+0.16 \left(\begin{smallmatrix} +0.10 \\ -0.06 \end{smallmatrix} \right)$	$+0.05 (\pm 0.09)$	$+0.15 \left(\begin{smallmatrix} +0.09 \\ -0.06 \end{smallmatrix} \right)$	$+0.05 (\pm 0.09)$
$\Delta\text{Weighting}$	$-0.011 \left(\begin{smallmatrix} +0.05 \\ -0.09 \end{smallmatrix} \right)$	$+0.01 (\pm 0.05)$	$+0.06 \left(\begin{smallmatrix} +0.10 \\ -0.12 \end{smallmatrix} \right)$	$+0.01 (\pm 0.06)$	$+0.06 \left(\begin{smallmatrix} +0.09 \\ -0.12 \end{smallmatrix} \right)$	$+0.006 (\pm 0.06)$	$+0.06 \left(\begin{smallmatrix} +0.09 \\ -0.12 \end{smallmatrix} \right)$
$\Delta\text{Fit priors}$	$+0.04 \left(\begin{smallmatrix} +0.05 \\ -0.02 \end{smallmatrix} \right)$	$+0.07 (\pm 0.06)$	$+0.05 (\pm 0.09)$	$+0.09 \left(\begin{smallmatrix} +0.10 \\ -0.05 \end{smallmatrix} \right)$	$+0.04 (\pm 0.07)$	$+0.04 (\pm 0.06)$	$+0.04 \left(\begin{smallmatrix} +0.09 \\ -0.12 \end{smallmatrix} \right)$
$\Delta\text{Instrument}$	$+0.01 \left(\begin{smallmatrix} +0.10 \\ -0.02 \end{smallmatrix} \right)$	$+0.10 \left(\begin{smallmatrix} +0.10 \\ -0.07 \end{smallmatrix} \right)$	$-0.087 \left(\begin{smallmatrix} +0.08 \\ -0.10 \end{smallmatrix} \right)$	$+0.11 \left(\begin{smallmatrix} +0.11 \\ -0.09 \end{smallmatrix} \right)$	$-0.087 \left(\begin{smallmatrix} +0.07 \\ -0.09 \end{smallmatrix} \right)$	$+0.11 \left(\begin{smallmatrix} +0.10 \\ -0.07 \end{smallmatrix} \right)$	$-0.086 (\pm 0.09)$
ΔStars	$+0.12 (\pm 0.33)$	$+0.00 \left(\begin{smallmatrix} +0.08 \\ -0.06 \end{smallmatrix} \right)$	$+0.01 \left(\begin{smallmatrix} +0.18 \\ -0.26 \end{smallmatrix} \right)$	$+0.00 \left(\begin{smallmatrix} +0.12 \\ -0.06 \end{smallmatrix} \right)$	$+0.01 \left(\begin{smallmatrix} +0.17 \\ -0.25 \end{smallmatrix} \right)$	$-0.018 \left(\begin{smallmatrix} +0.11 \\ -0.06 \end{smallmatrix} \right)$	$+0.02 \left(\begin{smallmatrix} +0.17 \\ -0.25 \end{smallmatrix} \right)$
$\Delta\text{Distance}$	$\pm 0.04 \left(\begin{smallmatrix} +0.04 \\ -0.05 \end{smallmatrix} \right)$	$+0.03 (\pm 0.06)$	$+0.02 (\pm 0.08)$	$+0.04 (\pm 0.06)$	$+0.02 (\pm 0.08)$	$\pm 0.03 \left(\begin{smallmatrix} +0.06 \\ -0.05 \end{smallmatrix} \right)$	$+0.02 (\pm 0.08)$
$\Delta\text{Fit radius}$	$+0.01 \left(\begin{smallmatrix} +0.05 \\ -0.04 \end{smallmatrix} \right)$	$-0.09 (\pm 0.11)$	$-0.072 \left(\begin{smallmatrix} +0.09 \\ -0.12 \end{smallmatrix} \right)$	$+0.10 (\pm 0.12)$	$-0.068 \left(\begin{smallmatrix} +0.08 \\ -0.12 \end{smallmatrix} \right)$	$+0.09 \left(\begin{smallmatrix} +0.13 \\ -0.10 \end{smallmatrix} \right)$	$-0.076 \left(\begin{smallmatrix} +0.09 \\ -0.11 \end{smallmatrix} \right)$
$\Delta\text{Covariance}$	$-0.019 (\pm 0.06)$	$+0.01 \left(\begin{smallmatrix} +0.06 \\ -0.07 \end{smallmatrix} \right)$	$-0.015 (\pm 0.10)$	$+0.02 \left(\begin{smallmatrix} +0.06 \\ -0.08 \end{smallmatrix} \right)$	$-0.020 \left(\begin{smallmatrix} +0.11 \\ -0.08 \end{smallmatrix} \right)$	$+0.01 (\pm 0.06)$	$-0.022 \left(\begin{smallmatrix} +0.12 \\ -0.08 \end{smallmatrix} \right)$

NOTE. — Marginalized values and $1\text{-}\sigma$ confidence regions for the stellar mass-to-light (M_*/L_K) ratio and the enclosed mass and concentration measured at various overdensities. Since the best-fitting parameters need not be identical to the marginalized values, we also list the best-fitting values for each parameter (in parentheses). In addition to the statistical errors, we also show estimates of the error budget from possible sources of systematic uncertainty. We consider a range of different systematic effects, which are described in detail in § 5; specifically we evaluate the effect of the choice of dark matter halo model (ΔDM), adiabatic contraction (ΔAC), treatment of the background ($\Delta\text{Background}$) and the Solar wind charge exchange X-ray component (ΔSWCX), the extrapolation of the entropy model ($\Delta\text{Entropy}$), deprojection (Δ3d), the employed spectral model ($\Delta\text{Spectral}$), removing the emissivity correction ($\Delta\text{Weighting}$), varying the priors on the model parameters ($\Delta\text{Fit priors}$) the X-ray detectors used ($\Delta\text{Instrument}$), the modelling of the stellar light (ΔStars), distance uncertainties ($\Delta\text{Distance}$), fit radius ($\Delta\text{Fit radius}$) and covariance between the temperature and density data-points ($\Delta\text{Covariance}$). We list the change in the marginalized value of each parameter for every test and, in parentheses, the statistical uncertainty on the parameter determined from the test. Note that the systematic error estimates should *not* in general be added in quadrature with the statistical error.

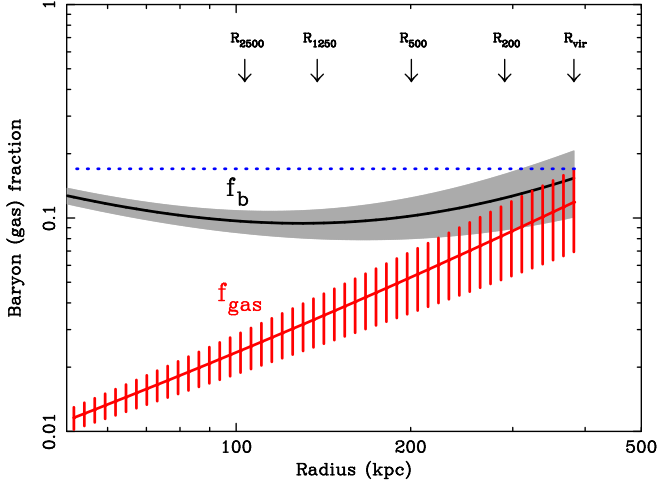


FIG. 9.— Baryon fraction profile inferred from our best-fitting models (black line). The shaded grey region indicates the $1\text{-}\sigma$ statistical uncertainty in the fits. The red shaded region indicates the gas fraction profile and $1\text{-}\sigma$ uncertainty. The dotted line indicates the best-fitting Cosmological value of f_b , based on the 5-year WMAP data (Dunkley et al. 2009), which lies significantly above the measured f_b for most of the radial range. We indicate the physical scales corresponding to R_{vir} and various other standard radii.

of radius, and we tabulate the gas fraction (f_g) and f_b , measured at different over-densities, in Table 4. Outside ~ 100 kpc ($\sim R_{2500}$), our model predicts that the f_b pro-

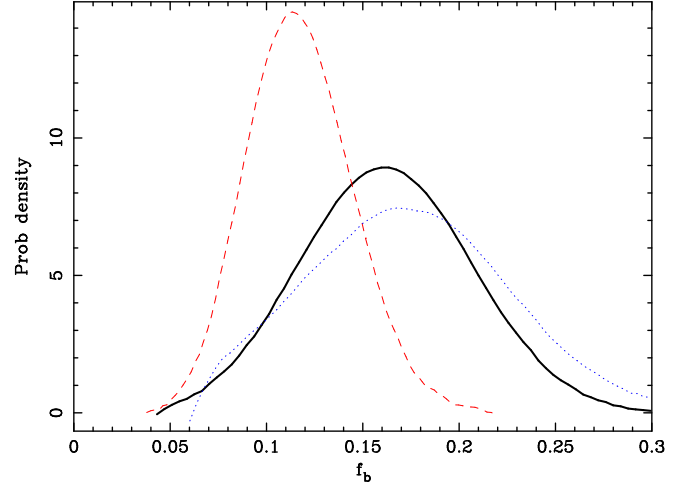


FIG. 10.— Marginalized probability density for $f_{b,\text{vir}}$ for different choices of the extrapolated entropy profile. The solid (black) line is for the default case, where we extrapolate the measured entropy profile to R_{vir} . As shown in § 6.4, this extrapolation is consistent with trends seen in massive galaxy clusters. Also shown are the cases where we allow the entropy profile to break at ~ 80 kpc, and the logarithmic slope (γ) is much steeper ($\gamma = 2.5$; dashed red line) or flatter ($\gamma = 0.0$; blue dotted line). For clarity, we smoothed the distribution functions with a fourth-order Savitzky-Golay filter, which spans $\sim 25\%$ of the measured f_b range. Although the best-fitting values depend to some degree on this choice (see also § 5.3), in all cases $f_{b,\text{vir}}$ is close to the Cosmological value (0.17).

TABLE 4
BARYON FRACTION RESULTS AND ERROR BUDGET

Test	$f_{g,2500}$	$f_{g,500}$	$f_{g,vir}$	$f_{b,2500}$	$f_{b,500}$	$f_{b,vir}$
Marginalized	$0.027^{+0.003}_{-0.004}$	$0.06^{+0.009}_{-0.02}$	$0.12^{+0.05}_{-0.03}$	0.10 ± 0.01	$0.11^{+0.02}_{-0.02}$	0.16 ± 0.04
Best-fit	(0.024)	(0.053)	(0.119)	(0.096)	(0.102)	(0.154)
Systematic error estimates						
Δ DM profile	$-0.004 (\pm 0.003)$	$-0.024 (\pm 0.01)$	$-0.085 \begin{pmatrix} +0.01 \\ -0.01 \end{pmatrix}$	$-0.013 (\pm 0.01)$	$-0.044 (\pm 0.01)$	$-0.114 (\pm 0.01)$
Δ AC	$-0.001 (\pm 0.004)$	$-0.010 \begin{pmatrix} +0.01 \\ -0.01 \end{pmatrix}$	$-0.019 \begin{pmatrix} +0.05 \\ -0.03 \end{pmatrix}$	$-0.026 (\pm 0.01)$	$-0.023 (\pm 0.02)$	$-0.035 (\pm 0.04)$
Δ Background	$-0.003 (\pm 0.003)$	$-0.001 (\pm 0.01)$	$+0.03 (\pm 0.04)$	$-0.005 \begin{pmatrix} +0.01 \\ -0.01 \end{pmatrix}$	$\pm 0 (\pm 0.02)$	$+0.02 \begin{pmatrix} +0.04 \\ -0.03 \end{pmatrix}$
Δ SWCX	$\pm 0 (\pm 0.002)$	$+0.001 \begin{pmatrix} +0.01 \\ -0.01 \end{pmatrix}$	$+0.03 \begin{pmatrix} +0.03 \\ -0.04 \end{pmatrix}$	$+0.003 (\pm 0.01)$	$+0.005 (\pm 0.01)$	$+0.03 \begin{pmatrix} +0.03 \\ -0.04 \end{pmatrix}$
Δ Entropy	$\pm 0 (\pm 0.004)$	$-0.018 (\pm 0.01)$	$+0.02 \begin{pmatrix} +0.02 \\ -0.04 \end{pmatrix}$	$\pm 0 (\pm 0.01)$	$+0.01 \begin{pmatrix} +0.01 \\ -0.01 \end{pmatrix}$	$+0.01 \begin{pmatrix} +0.01 \\ -0.05 \end{pmatrix}$
Δ 3d	$+0.005 \begin{pmatrix} +0.004 \\ -0.005 \end{pmatrix}$	$+0.010 (\pm 0.02)$	$+0.04 \begin{pmatrix} +0.05 \\ -0.08 \end{pmatrix}$	$+0.01 (\pm 0.01)$	$+0.01 (\pm 0.03)$	$+0.03 \begin{pmatrix} +0.06 \\ -0.08 \end{pmatrix}$
Δ Spectral	$+0.001 \begin{pmatrix} +0.001 \\ -0.008 \end{pmatrix}$	$-0.026 (\pm 0.01)$	$+0.02 \begin{pmatrix} +0.01 \\ -0.07 \end{pmatrix}$	$+0.00 \begin{pmatrix} +0.01 \\ -0.03 \end{pmatrix}$	$+0.01 \begin{pmatrix} +0.01 \\ -0.04 \end{pmatrix}$	$+0.03 \begin{pmatrix} +0.03 \\ -0.09 \end{pmatrix}$
Δ Weighting	$-0.001 (\pm 0.002)$	$\pm 0 (\pm 0.01)$	$+0.01 (\pm 0.05)$	$-0.006 (\pm 0.01)$	$-0.003 (\pm 0.01)$	$+0.008 (\pm 0.05)$
Δ Fit priors	$+0.007 \begin{pmatrix} +0.007 \\ -0.004 \end{pmatrix}$	$+0.01 \begin{pmatrix} +0.01 \\ -0.02 \end{pmatrix}$	$+0.02 \begin{pmatrix} +0.06 \\ -0.05 \end{pmatrix}$	$+0.01 \begin{pmatrix} +0.01 \\ -0.01 \end{pmatrix}$	$\pm 0.02 (\pm 0.02)$	$+0.01 \begin{pmatrix} +0.01 \\ -0.06 \end{pmatrix}$
Δ Instrument	$-0.008 (\pm 0.005)$	$-0.025 (\pm 0.02)$	$-0.067 (\pm 0.06)$	$-0.021 (\pm 0.01)$	$-0.032 (\pm 0.02)$	$-0.081 (\pm 0.05)$
Δ Stars	$\pm 0 (\pm 0.004)$	$-0.006 \begin{pmatrix} +0.02 \\ -0.01 \end{pmatrix}$	$+0.008 (\pm 0.05)$	$+0.02 \begin{pmatrix} +0.03 \\ -0.01 \end{pmatrix}$	$-0.008 \begin{pmatrix} +0.03 \\ -0.02 \end{pmatrix}$	$+0.01 \begin{pmatrix} +0.05 \\ -0.06 \end{pmatrix}$
Δ Distance	$-0.002 \begin{pmatrix} +0.004 \\ -0.003 \end{pmatrix}$	$-0.007 \begin{pmatrix} +0.02 \\ -0.01 \end{pmatrix}$	$+0.001 \begin{pmatrix} +0.05 \\ -0.04 \end{pmatrix}$	$-0.00 \begin{pmatrix} +0.02 \\ -0.00 \end{pmatrix}$	$-0.006 \begin{pmatrix} +0.02 \\ -0.02 \end{pmatrix}$	$-0.006 (\pm 0.05)$
Δ Fit radius	$-0.007 \begin{pmatrix} +0.007 \\ -0.005 \end{pmatrix}$	$-0.019 (\pm 0.02)$	$-0.064 \begin{pmatrix} +0.07 \\ -0.04 \end{pmatrix}$	$-0.017 (\pm 0.02)$	$-0.032 \begin{pmatrix} +0.03 \\ -0.02 \end{pmatrix}$	$-0.076 \begin{pmatrix} +0.08 \\ -0.04 \end{pmatrix}$
Δ Covariance	$-0.002 \begin{pmatrix} +0.004 \\ -0.003 \end{pmatrix}$	$-0.005 (\pm 0.01)$	$+0.02 \begin{pmatrix} +0.04 \\ -0.06 \end{pmatrix}$	$+0.002 (\pm 0.01)$	$\pm 0.00 (\pm 0.02)$	$+0.003 (\pm 0.05)$

NOTE. — Marginalized values and $1\text{-}\sigma$ confidence regions for the gas fraction ($f_{g,\Delta}$) and baryon fraction ($f_{b,\Delta}$) measured at various overdensities (Δ). We also provide the best-fitting parameters in parentheses, and a breakdown of possible sources of systematic uncertainty, following Table 3. We find that f_b is reasonably robust to most sources of systematic uncertainty, especially within R_{2500} .

file rises gently, from $\sim 10\text{--}15\%$. In Fig 10 we show the posterior probability density function for $f_{b,vir}$ (f_b extrapolated to R_{vir}), which is tightly constrained to around $\sim 15\%$, very close to the Cosmological value. A potentially important source of uncertainty in this extrapolation is the shape of the entropy profile. In Fig 10 we show the equivalent posterior probability density functions for two different entropy extrapolations, which should bound all likely entropy profiles. We discuss these fits in detail in § 5.3. Clearly, uncertainties the entropy extrapolation do not produce a large systematic shift in our inferred $f_{b,vir}$.

5. SYSTEMATIC ERROR BUDGET

In this section, we address the sensitivity of our results to various data analysis choices that were made, including the choice of prior. In most cases, it is difficult or impractical to express these assumptions through a single additional model parameter over which one might hope to marginalize, and so we adopted the pragmatic approach of investigating how our results changed if the assumptions were arbitrarily adjusted. We focused on those systematic effects likely to have the greatest impact on our conclusions, and list in Tables 3 and 4 the change to the marginalized value of each key parameter for each test. We outline below how each test was performed. Those readers uninterested in the technical details of our analysis may wish to proceed directly to Section 6

5.1. Dark Matter profile

One of the major sources of uncertainty on the recovered f_b is the choice of DM mass model. While our default model (NFW) is theoretically motivated,

and supported by observations of galaxy clusters (e.g. Vikhlinin et al. 2006), we also experimented with a so-called “cored logarithmic” mass model, which has been widely used in studies of elliptical galaxies (Binney & Tremaine 2008), including some recent stellar dynamical studies (e.g. Thomas et al. 2007b; Gebhardt & Thomas 2009). This model tends to predict higher masses at large radii than NFW, resulting in a significantly larger M_{vir} , and correspondingly a smaller value of f_b when extrapolated within R_{vir} . Nevertheless, at radii corresponding to higher mass overdensities, the extrapolation range is smaller and the discrepancy is significantly reduced, so that the choice of DM model has little effect on $f_{b,2500}$ (“ Δ DM profile” in Tables 3 and 4). In any case, we note that the cored logarithmic model is less well-motivated theoretically than the NFW profile. Furthermore, we find that the data slightly favour the NFW model; although the best-fitting χ^2 is comparable between the two cases, the ratio of the Bayesian evidence is $\sim 1.5 \times 10^{-4}$, implying that the cored logarithmic model, with the adopted priors (a flat prior on the asymptotic circular velocity, between 10 and 2000 $km s^{-1}$, and a flat prior on $\log_{10} r_c$, where r_c is the core radius, over the range $0 \leq \log_{10} r_c \leq 3$.) is a poorer description of the data at $\sim 3.8\text{-}\sigma$.

One modification to the (NFW) DM profile shape that is theoretically predicted is “adiabatic contraction” (Blumenthal et al. 1986; Gnedin et al. 2004), where the DM halo density profile reacts to the gravitational influence of baryons that are condensing into stars by becoming cuspier. There is little observational evidence of this effect (e.g. H06; Humphrey et al. 2009a; Gnedin et al. 2007; although, see Napolitano et al. 2010), and it may be overestimated by existing models (Abadi et al. 2009), so we

did not employ it in our default analysis. Nevertheless, we experimented with modifying the NFW halo profile to account for this effect with the algorithm described by Gnedin et al. (2004)¹⁷. The principal effect of this modification was to lower slightly the stellar M/L ratio and, consequently, the inferred f_b (“ ΔAC ” in Tables 3 and 4).

5.2. Background

Our treatment of the background is a potentially serious source of systematic error. To investigate this, we adopted an alternative approach in which we used, for the *Chandra* data, the standard blank-field events files distributed with the CALDB to extract a background spectrum for each annulus. Since the blank-field files for each CCD have different exposures, spectra were accumulated for each CCD individually, scaled to a common exposure time and then added. The spectra were renormalized to match the observed count-rate in the 9–12 keV band. These “template” spectra were then used as a background in *Xspec*, and the background model components were omitted from our fit. We found that this approach gave a poorer fit to the data than the full modelling procedure used by default, and the overall density and temperature profiles were noticeably affected at large radii. For the *Suzaku* data, there are no blank-fields files available, but we used the standard non X-ray background spectra generated by *xisnxbgen* tool to remove the instrumental background, but maintained the sky background model components in our fit. Fitting the resulting *Chandra* and *Suzaku* temperature and density profiles with our mass modelling apparatus, our results were not substantially affected (“ $\Delta Background$ ” in Tables 3 and 4).

5.2.1. Solar Wind Charge Exchange

An additional background component can arise from the interaction of the Solar wind with interstellar material and the Earth’s exosphere. This should manifest itself as a time-variable, soft component that can be modelled as a series of narrow Gaussian lines, the intensity of which correlate with the Solar wind activity (e.g. Snowden et al. 2004). In the interests of minimizing the complexity of the spectral models, we do not by default explicitly account for this so-called “Solar wind charge exchange” (SWCX) in our fits. To some degree this component is degenerate with the sky background, which we fitted in our modelling, and so this omission may not be a significant source of bias in our analysis. Nevertheless, it is important to confirm that it is not.

To assess the contamination from the SWCX component, we first identified periods of low Solar wind proton flux, as measured by the Solar Wind Electron Proton Alpha Monitor (SWEPAM) instrument aboard the Advanced Composition Explorer (ACE) spacecraft (McComas et al. 1998)¹⁸. Following Snowden et al. (2004), we assumed the SWCX component is negligible for a Solar wind proton flux level $\lesssim 3 \times 10^8 \text{ cm}^{-2} \text{ s}^{-1}$. Selecting only times for which SWEPAM measured a proton flux

below this limit, we were left with ~ 145 ks of *Suzaku* data. Still, since the proton flux was only mildly enhanced during the (short) excluded periods, we found that the soft (0.5–1.0 keV) X-ray count-rate was only enhanced by a few percent in the entire (i.e. unfiltered) data as compared to the quiescent period. We found that there was very poor SWEPAM coverage of the periods during which the *Chandra* data were taken, and so we did not attempt to filter the *Chandra* data in the same way. Instead we modified the sky background component by adding a number of narrow Gaussian lines (fixed at the energies reported for the SWCX component by Snowden et al.).

The corrected *Chandra* and *Suzaku* spectra were fitted to obtain the temperature and density profiles, and folded through our mass modelling apparatus. We found that our results were not substantially affected by correcting for the SWCX component (“ $\Delta SWCX$ ” in Tables 3 and 4).

5.3. Entropy profile extrapolation

The extrapolation of the entropy profile is one of the prime sources of uncertainty in our determination of f_b at large scales. As we will show in § 6.4, our default profile is, in fact, consistent with trends seen in massive galaxy clusters (Pratt et al. 2010), giving us confidence in its use. Nevertheless, it is important to explore plausible alternative shapes. Motivated by observed entropy profiles in galaxy groups and by the monotonically rising entropy profiles required by hydrostatic equilibrium, we investigated two pathological extrapolations that should bound any plausible model. Specifically, we adopted a powerlaw shape (entropy $\propto R^\gamma$) outside ~ 80 kpc, with $\gamma = 0$ (i.e. a flat entropy profile), which is a secure lower boundary assuming stability against convection, or $\gamma = 2.5$. This latter value was chosen arbitrarily, and is far larger than has been observed in real systems. This choice primarily affects the extrapolated temperature, rather than the density profile, and so f_b does not change substantially with these choices (“ $\Delta Entropy$ ” in Tables 3 and 4; Fig 10).

5.4. Deprojection

In the present work, we opted to fit the projected, rather than the deprojected data (as done, for example, in H06). In general, fitting the projected data leads to smaller statistical error bars, but potentially larger systematic uncertainties (e.g. Gastaldello et al. 2007b), and so it is important to investigate the likely magnitude of such errors. To do this, we examined the effect on our results of spherically deprojecting the data. We achieved this by using the *Xspec project* model¹⁹. To account for emission projected into the line of sight from regions outside the outermost annulus, we added an apec plasma model to each annulus, with abundance 0.3 (consistent with the outermost annulus) and the temperature and normalization determined from projecting onto the line of sight the best-fitting gas temperature and density

¹⁷ Using the CONTRA code publicly available from <http://www.astro.lsa.umich.edu/~ognedin/contra/>

¹⁸ Based on the publicly released data available from <http://www.srl.caltech.edu/ACE/ASC/index.html>

¹⁹ In practice, it was more convenient to emulate the behaviour of *project* by adding multiple “vapec” plasma models in each annulus, with the relative normalizations tied appropriately (e.g. Kriss et al. 1983). This allowed data from the multiple *Suzaku* instruments to be fitted simultaneously.

models described in § 4.2, but considering the models only outside ~ 70 kpc.

Although the error-bars were increased when using the deprojected (rather than the projected) profiles (“ Δ Deprojection” in Tables 3 and 4), the best-fitting results were not significantly changed. In Fig 6, we show a series of mass “data-points” obtained from the deprojected density and temperature profiles, using the “traditional” mass analysis method described in Humphrey et al. (2009a, see also Humphrey & Buote 2010). These data agree very well with the best-fitting mass model found in our projected analysis. Similarly, the entropy profile derived directly from the deprojected data agrees well with the results of our projected analysis (Fig 5).

5.5. Priors

Since the choice of priors on the various parameters is arbitrary in our analysis, it is important to determine to what extent they could affect our conclusions. To do this, we replaced each arbitrary choice in turn with an alternative, reasonable prior. Specifically, for each parameter describing the entropy profile, we switched from a flat prior on that parameter to a flat prior on its logarithm. We replaced the flat prior on the stellar M/L ratio with a Gaussian prior, the mean and σ of which were determined from the stellar population synthesis model results reported in H06. We used a flat prior on the DM halo mass, rather than on its logarithm, and, instead of the flat prior on $\log c_{DM}$, we adopted the distribution of c around M found by either Buote et al. (2007) or Macciò et al. (2008) as a (Gaussian) prior. The effect of these choices is no larger than the statistical errors on each parameter, especially for the baryon fraction measured at R_{200} or higher overdensities (“ Δ Fit priors” in Tables 3 and 4).

5.6. Stellar light

As discussed in H06, careful treatment of the stellar light is essential for obtaining an accurate measurement of the gravitating mass profile. Since the stellar light deprojection is not unique, in particular as the inclination angle is not *a priori* known for an elliptical galaxy, we investigated the associated systematic uncertainty by first varying it within reasonable limits (§ 3). Specifically, we lowered it as far as 70° , since the highly elliptical projected isophotes of NGC 720 make it unlikely to be observed at a much lower inclination. As a more extreme test of the influence of the stellar light on our fits, we also experimented with excluding all the data within the central ~ 4 kpc, where the stars dominate the mass profile. We find that the stellar M/L ratio becomes (unsurprisingly) much more uncertain when we adopt this approach, but the best-fitting masses and f_b were not substantially affected (“ Δ Stars” in Tables 3 and 4).

5.7. Emissivity correction

In our default analysis, the projected temperature and density profile are weighted by the gas emissivity, folded through the instrumental responses (for details, see Appendix B of Gastaldello et al. 2007b). Since the computation of the gas emissivity assumes that the three dimensional gas abundance profile is identical to the projected profile (which is unlikely to be true), it is important to

assess how sensitive our conclusions are to the emissivity correction. To do this, we adopted the extreme approach of ignoring the spatial variation of the gas emissivity altogether. We found that this had a very small effect on our results (Δ Emissivity in Tables 3 and 4).

5.8. Remaining tests

We here outline the remaining tests we carried out, as summarized in Tables 3 and 4. First of all, since the inter-calibration of the *Suzaku* XIS units may not be perfect, we experimented with using only one of the units in the *Suzaku* analysis, and cycled through each choice. We found that the XIS1 (back-illuminated) unit appeared most inconsistent with the *Chandra* data, and so also investigated using only units 0, 2 and 3. We also considered using only the *Chandra* data. While these choices had a significant effect on $f_{b,vir}$, we found that f_b at higher overdensities was more resilient (“ Δ Instrument”).

To assess the impact of various spectral-fitting data analysis choices on our results, in turn we varied the neutral hydrogen column density by $\pm 25\%$, performed the fit over a restricted energy range (0.7–7.0 keV, or 0.5–4.0 keV), and replaced the APEC plasma model with a MEKAL model. The impact of these choices is comparable to the statistical errors on the parameters (“ Δ Spectral”).

To examine the error associated with distance uncertainties, we varied the distance to NGC 720 by the $1-\sigma$ error given in Tonry et al. (2001). The effect on our results is minor (“ Δ Distance”). To examine the sensitivity of our fits to the radial range studied, we excluded the data outside ~ 40 kpc. This exclusion made the extrapolation more uncertain, especially for $f_{b,vir}$ (“ Δ Fit radius”). Finally, to examine the possible errors associated with our treatment of the covariance between the density data-points, we investigated adopting a more complete treatment that considers the covariance between all the temperature and density data-points, as well as adopting the more standard (but incorrect) approach of ignoring the covariance altogether. The effect is not large (“ Δ Covariance” in Tables 3 and 4; Fig 8).

6. DISCUSSION

The combination of the new, high quality data for NGC 720 and our updated, Bayesian hydrostatic modelling procedure has greatly improved our constraints on its gravitating matter and hot ISM. We here discuss the implications of these new measurements at some length.

6.1. Hydrostatic equilibrium

The ability of our hydrostatic model to reproduce the temperature and density profiles of the gas in NGC 720 strongly suggests that the gas is close to hydrostatic; despite highly nontrivial temperature and density profiles, a smooth, physical mass model and a monotonically rising entropy profile (required for stability against convection) were able to reproduce them well. If the hydrostatic approximation is seriously in error, this would require a remarkable conspiracy between the temperature and density data points. The closeness of the system to hydrostatic is unsurprising given its remarkably relaxed X-ray morphology (Fig 1; Buote et al. 2002; Buote & Canizares 1996, 1994) and lack of substantial radio emission (Fabiano et al. 1987). Numerical simulations of structure

formation suggest that deviations from hydrostatic equilibrium in morphologically relaxed-looking systems are not large, so that errors in the recovered mass distribution should be no larger than $\sim 25\%$ (e.g. Tsai et al. 1994; Buote & Tsai 1995; Nagai et al. 2007; Piffaretti & Valdarnini 2008; Fang et al. 2009). Such a level of non-thermal support is comparable to the $\sim 10\text{--}20\%$ discrepancy found between X-ray and stellar dynamical mass measurements by Churazov et al. (2008) for two galaxies that are manifestly more disturbed than NGC 720.

In the case of NGC 720, there is additional, albeit circumstantial, evidence which supports the hydrostatic approximation. First, the best-fitting virial mass is in good agreement with the modest (although uncertain) velocity dispersion of the dwarf companions about NGC 720, ($117 \pm 54 \text{ km s}^{-1}$, corresponding to a virial mass of $4 \pm 4 \times 10^{12} M_{\odot}$; Brough et al. 2006). In our studies of other systems, we have used the good correspondence between the measured stellar M/L ratio and that predicted by single-burst stellar population synthesis (SSP) models that assume a Kroupa (2001) IMF, to infer that there is little nonthermal pressure (Humphrey et al. 2009a). In the case of NGC 720, the measured M/L_K ratio (0.54 ± 0.05) is actually *higher* than the predictions of the SSP models (0.35 ± 0.07 : H06). A natural way to bring these results into agreement is if the young ($\sim 3 \text{ Gyr}$: Humphrey & Buote 2006; Rembold et al. 2005) stellar population that dominates the light only represents recent star-formation superimposed on an older, underlying stellar population with a higher M/L_K ratio. Such a picture is supported by the multiple-aged stellar population inferred by Rembold et al. (2005). We note that the measured M/L_K value could also be reconciled with the predictions of SSP models if a Salpeter IMF is adopted (for which M/L_K ~ 0.54 ; taken in the context of our previous work this would indicate a non-universal IMF). Alternatively, if AC operates, making NGC 720 unique amongst the systems we have studied in the X-ray, the measured M/L_K would be 0.39 ± 0.04 , also reconciling the fit result and the SSP predictions. While it is evidently difficult to draw strong conclusions based on the M/L_K ratio, none of these arguments indicates that the measured M/L_K is obviously underestimated. This is important since most models predict that non-hydrostatic effects lead to an *underestimate* of the mass (e.g. Nagai et al. 2007; Churazov et al. 2008; Fang et al. 2009).

Humphrey & Buote (2010) studied NGC 720, as part of a sample of galaxies, groups and clusters, finding that the total gravitating mass profile in the central region ($\lesssim 30 \text{ kpc}$) is close in shape to a singular isothermal sphere distribution. This shape is what is approximately inferred from lensing plus stellar dynamics studies of similar galaxies (e.g. Koopmans et al. 2009). Therefore, any deviations from hydrostatic equilibrium are unlikely to have substantially affected the overall shape of the gravitating mass profile, at least over this region. Nevertheless, it is plausible that a constant fraction of the pressure over this region comes from nonthermal effects, which would just reduce the overall normalization of the measured mass model. Such a scenario would imply that the true R_{vir} is underestimated, while the scale radius is approximately correct; hence c_{vir} would be underestimated,

putting it in more tension with theory. Conversely, it is unlikely that deviations from hydrostatic equilibrium could lead to the scale radius also being underestimated, since that would require the nonthermal pressure support to increase dramatically outside $\sim 20 \text{ kpc}$. Since NGC 720 is an isolated system, it is difficult to imagine what processes could give rise to such an effect.

One effect which could produce deviations from hydrostatic equilibrium at the smallest scales is gas rotation induced by spin-up of subsonically inflowing gas. Considering the very relaxed galaxy NGC 4649 Brighenti et al. (2009) demonstrated that angular momentum conservation (if there is appreciable rotation in the stars) flattens the X-ray ellipticity significantly in the centre of the system (where deviations from hydrostatic equilibrium are also most significant). NGC 720 exhibits sufficient major-axis rotation (Binney et al. 1990), but only a hint of a central ellipticity rise within the innermost $\sim 1 \text{ kpc}$ (Buote et al. 2002). Since our results are not very sensitive to the exclusion of data within the central $\sim 4 \text{ kpc}$ (§ 5.8), it seems unlikely that this effect could have an impact on our results, even if it is operating in NGC 720.

Our conclusions on the state of hydrostatic equilibrium in NGC 720 differ significantly from those of Diehl & Statler (2007). Those authors investigated the X-ray and optical isophotal ellipticities at a fixed, small scale in an heterogeneous sample of early-type galaxies, concluding that the lack of a correlation between them (in conflict with what would be expected if hydrostatic equilibrium holds exactly) indicates that hydrostatic equilibrium is not ubiquitous and, therefore, should never be assumed (even approximately) in mass analysis (and, in particular, for NGC 720). We consider their conclusions, however, to be extreme and misleading. Firstly, their method does not allow them to say anything at all about individual objects, and only indicates that hydrostatic equilibrium is unlikely to hold *perfectly* in a galaxy randomly drawn from their sample, provided it is *chosen without any consideration of its morphology*. Since their sample contained galaxies with such large-scale asymmetries that we would not recommend the routine application of hydrostatic mass methods (e.g. NGC 4636: Jones et al. 2002 and M 84: Finoguenov & Jones 2001), and since they focused on the smallest scales (where X-ray point-source removal is most challenging and where AGN-driven disturbances are most serious), in contrast to the large scales that are most important for dark matter analysis, the implications for morphologically relaxed systems such as NGC 720 or NGC 4649 (Humphrey et al. 2008) are unclear. Secondly, even if it does not hold *perfectly*, hydrostatic equilibrium can still be a useful approximation. With their hydrodynamical models, Brighenti et al. (2009) reconciled the X-ray and optical ellipticity profiles of NGC 4649 by requiring modest gas motions, but the gas remained very close to hydrostatic (especially outside the innermost $\sim 1 \text{ kpc}$). Substantial non-hydrostatic gas motions are likely to manifest themselves as sharp features in the surface brightness and temperature profiles of the hot gas, for example those seen in the core of M 87 (Forman et al. 2007; Million et al. 2010). Still, even for M 87, Churazov et al. (2008) found that the gas was close to hydrostatic away from the regions of most significant disturbance. In the case

of NGC 720, the profiles are significantly smoother than in M 87 (Fig 3), while the hydrostatic isophotal analysis undertaken by Buote et al. (2002) found evidence for a dark matter halo ellipticity in excellent agreement with the predictions of cosmological models (implying the gas is not grossly out of equilibrium). In summary, in our detailed analysis of NGC 720 and other systems (Humphrey et al. 2009a; Brighenti et al. 2009), we find no evidence supporting Diehl & Statler’s contention that hydrostatic equilibrium is a very poor approximation in morphologically relaxed galaxies (which seems little more than “guilt by association”).

6.2. Baryon fraction

6.2.1. Robustness of f_b measurement

Based on our self-consistent hydrostatic mass model for NGC 720, and the fit to the density profile, we were able to obtain unprecedented f_b constraints in a galaxy-scale system at large radius. Since the current X-ray data only reach $\sim 0.7R_{2500}$ (with the field of view of *Suzaku* being the primary limiting factor), most of the constraints are based on an extrapolation. Nevertheless, this is done in a well-motivated, self-consistent manner, relying only on how the mass and entropy profiles behave at large radius, and the validity of the hydrostatic approximation at large scales. Of these, the dark matter halo mass profile has by far the biggest influence on the inferred f_b , as discussed in § 5.1. Specifically, $f_{b,\text{vir}}$ changes from ~ 0.15 when an NFW dark matter halo is adopted to ~ 0.04 for a “cored logarithmic” dark matter mass model, which mostly reflects the higher M_{vir} in the latter case. While this is a concern, the NFW model is much better motivated cosmologically, and supported observationally by high-quality X-ray and lensing studies of other (albeit more massive) systems (Lewis et al. 2003; Pointecouteau et al. 2005; Vikhlinin et al. 2006; Gavazzi et al. 2007). Still, even if the true DM mass model differs unexpectedly from NFW, we find that f_b measured within regions of larger overdensity (e.g. R_{2500}) is much less sensitive to this issue, reflecting the smaller range of extrapolation.

While the extrapolation of the entropy profile in our analysis is also a potential cause for concern, this choice does not significantly affect our conclusions (Fig 10). In fact, even allowing for a pathological variation in the slope of the entropy profile at large radius (γ ranging from 0–2.5), we find that the best-fitting $f_{b,\text{vir}}$ varies by only $\sim 1\text{-}\sigma$. This apparent lack of sensitivity to γ arises because changing the entropy distribution in our hydrostatic models tends to affect the implied temperature more strongly than the gas density.

Another factor which may complicate the extrapolated f_b values is the hydrostatic approximation. As we argued in § 6.1, there is good evidence to suggest the gas is hydrostatic within ~ 75 kpc, but we cannot directly assess the validity of this approximation at larger scales. Most mechanisms that can produce strong deviations from the single-phase, hydrostatic approximation in an isolated galaxy would actually provide non-thermal support to the gas (e.g. Zappacosta et al. 2006; Nagai et al. 2007; Churazov et al. 2008; Fang et al. 2009). This would produce a *flatter* gas density profile than the purely hydrostatic case, thereby *increasing* the actual baryon fraction over that inferred from our extrapola-

tion. (An exception is if the gas is globally outflowing, in which case the gas is over-pressured, and the hydrostatic model would over-estimate f_b . However, such a global outflow would have to be triggered by feedback from the central galaxy, so it seems implausible for there to be an outflow outside ~ 75 kpc, but no evidence of one at smaller scales.) Numerical cosmological simulations of hot halos around galaxies do, indeed, predict that they are quasi-hydrostatic (e.g. Crain et al. 2010).

Our measurement of f_b given in Table 4 does not include all of the baryons within the system, since it ignores the dwarf companions. In practice, the total K-band luminosity of the detected dwarf galaxies is only $\sim 10\%$ of that of NGC 720 (Brough et al. 2006), and the HI content of these galaxies is much smaller still (Sengupta et al. 2007; Kilborn et al. 2009). If the luminosity function of these galaxies is similar to that of Milky Way dwarfs, their combined luminosity will be dominated by the brightest few members (Tollerud et al. 2008), and so the baryons hosted by as yet undetected, fainter dwarfs will not significantly affect this estimate. Additional baryons could plausibly exist in a hard-to-detect extended stellar envelope, analogous to the “intra-cluster light” seen in clusters and massive groups, but galaxy formation models suggest that, for a system of this mass, at most $\sim 10\%$ of the total stellar mass could be distributed in this way (Purcell et al. 2007). Finally, we note that NGC 720 itself does not contain significant cool gas (Huchtmeier 1994; Welch et al. 2010). Failing to include these uncounted sources of baryons, therefore, may bias our inferred f_b values low by at most ~ 0.01 .

6.2.2. Implications

Based on our hydrostatic mass models, the total *stellar mass fraction* within R_{vir} is small ($\sim 0.035 \pm 0.003$), but in good agreement with that generally inferred from gravitational lensing studies of early-type galaxies (Hoekstra et al. 2005; Gavazzi et al. 2007). Most of the baryons within R_{vir} are, however, in the form of the hot gas. Including both gas and stars, the measured f_b profile is relatively flat at $\sim 0.10\text{--}0.15$ between R_{2500} and R_{vir} (Fig 9), becoming completely consistent with the Cosmological value (0.17: Dunkley et al. 2009) when extrapolated to R_{vir} . In H06 we reported a lower value of f_b within R_{vir} for NGC 720 (~ 0.04), based on simpler hydrostatic model fits to data from a much shallower *Chandra* observation. That constraint, however, was almost entirely driven by a strong prior that imposed a tight correlation between M_{vir} and f_b ; when relaxing this prior, we found that f_b was very poorly constrained by those data.

A number of authors have investigated the gas (or baryon) fraction in galaxy groups and clusters, typically finding a shallow dependence on the virial mass of the halo. In the upper panel of Fig 11 we show the gas fraction measurements within R_{2500} ($f_{g,2500}$) versus M_{2500} for the group and cluster samples of Vikhlinin et al. (2006), Gastaldello et al. (2007b) and Sun et al. (2009)²⁰. Overlaid is the locus of NGC 720, which is in good agreement of an extrapolation of the powerlaw trend inferred

²⁰ For clarity, we omit systems with large error-bars ($\sigma(f_g) \gtrsim 0.01$). Where the samples overlap, we use the results, in order of preference, from Gastaldello et al. (2007b) and Sun et al. (2009).

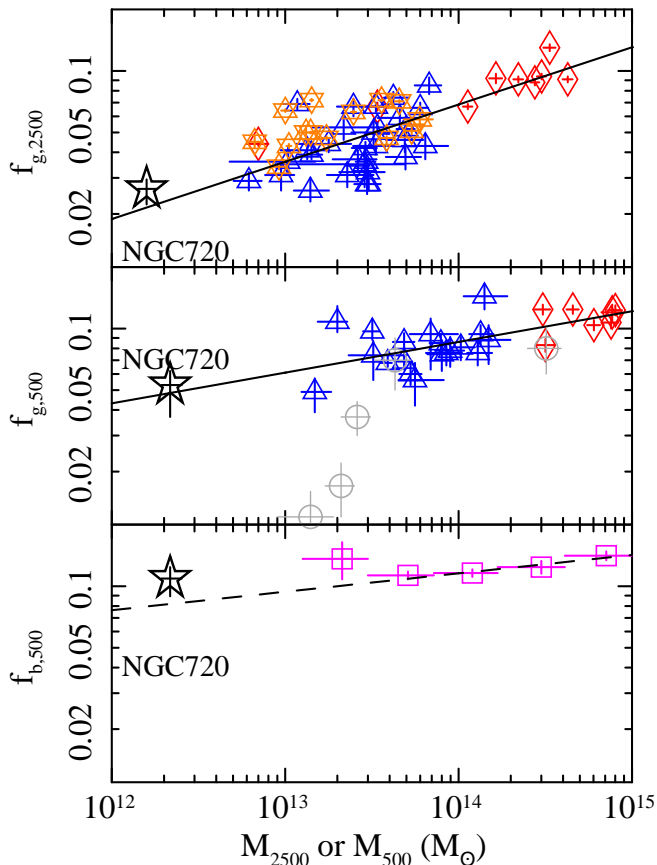


FIG. 11.— *Top panel:* Gas fraction within R_{2500} shown as a function of M_{2500} for the isolated galaxy NGC 720 (five-pointed star) and a literature sample of groups and clusters (Vikhlinin et al. 2006: diamonds; Gastaldello et al. 2007b: six-pointed stars; Sun et al. 2009: triangles). The best powerlaw fit to the data is shown as a solid line. The gas fraction within R_{2500} of NGC 720 is clearly consistent with an extrapolation of the trend for galaxy groups and clusters. *Centre panel:* The same, but within an overdensity of 500. We overlay additional literature data from Dai et al. (2009, circles). *Lower panel:* Baryon fraction within R_{500} as a function of M_{500} for NGC 720 and the mean data for the group and cluster sample of Giodini et al. (2009, squares). The best-fitting powerlaw relation from Giodini et al. is overlaid (dashed line). NGC 720 is clearly consistent with an extrapolation of this relationship to low masses.

for the more massive systems. Fitting a model of the form

$$\log_{10} f_g = A + B \log_{10} \left(\frac{M}{2 \times 10^{14} M_{\odot}} \right) \quad (3)$$

to these data, using a method that takes into account errors on both axes and intrinsic scatter in the y-direction (specifically, that employed in Humphrey & Buote 2008), we found $A = -1.08 \pm 0.03$ and $B = 0.28 \pm 0.04$, with an intrinsic scatter of 0.11 dex. In the centre panel of Fig 11, we show a similar comparison between $f_{g,500}$ and M_{500} , similarly finding that the locus of NGC 720 is consistent with an extrapolation of the trends for the massive systems. Fitting a log-linear regression line (Eqn 3), we obtained $A = -1.02 \pm 0.02$ and $B = 0.15 \pm 0.03$, with an intrinsic scatter of 0.06 dex, in good agreement with a fit by Giodini et al. (2009) to a similar group and cluster sample, but omitting the NGC 720 datapoint. Since the temperature varies only by ~ 1 order of magnitude for the almost 3 orders of magnitude mass range between the

galaxies and clusters, hydrostatic equilibrium generally requires that massive systems have a more rapidly declining gas density profile than less-massive objects, and hence a more centrally peaked gas mass distribution, as compared to the distribution of dark matter. Given this trend, it is not surprising that lower-mass objects have a smaller fraction of their total gas mass within R_{2500} , as indicated by the dependence of B on the overdensity.

Also shown in Fig 11 (centre panel) are a set of datapoints taken from Dai et al. (2009), who fitted stacked Rosat All-Sky Survey (RASS) data of optically selected galaxy groups and clusters. These points appear quite discrepant with this relation (and the other data) below $\sim 3 \times 10^{13} M_{\odot}$, where they fall sharply. This may indicate real differences in the properties of optically selected groups from those selected from X-ray surveys, but it may also reflect the significant systematic errors that are involved with stacking the RASS data (see Dai et al. 2007).

While the gas is the dominant baryonic component for the most massive clusters, the stellar-to-gas mass ratio is actually a strong function of M_{500} . In NGC 720, approximately half of the baryons within R_{500} are in the stars. Accounting for both gas and stars Giodini et al. (2009) obtained average f_b constraints within R_{500} for a galaxy group and cluster sample. In the lower panel of Fig 11, we show their data as a function of M_{500} , along with the best powerlaw fit to their data, and the locus of NGC 720. It is immediately clear that NGC 720 is in good agreement with the extrapolation of the (shallow) trend they observe to low masses. Dai et al. (2009) also reported total baryon fractions for their galaxy group and cluster sample, finding rather lower values of $f_{b,200}$ in their lowest mass systems ($f_{b,200} \sim 0.04$ at $M_{200} \sim 3 \times 10^{13} M_{\odot}$). This is significantly below $f_{b,200}$ observed in NGC 720 (which has M_{200} an order of magnitude lower), but is comparable to its stellar mass fraction. Still, as discussed above, the gas fraction estimates from their work appear discrepant with studies of X-ray selected groups and this may explain the inconsistency.

Our study of NGC 720 clearly demonstrates that it is possible for a system with M_{vir} as low as a few times $10^{12} M_{\odot}$ to retain a massive, quasi-hydrostatic hot halo. The total baryon fraction, when extrapolated to the virial radius, is consistent with the Cosmological value, indicating that massive dark matter halos around galaxies could be a significant reservoir for some fraction of the “missing baryons” (e.g. Fukugita & Peebles 2006). The biggest spiral galaxies are believed to reside in halos of comparable mass, making it particularly interesting to compare the hot halo around NGC 720 to those predicted around spiral galaxies. Intriguingly, the total gas content of the system (gas fraction within R_{200} of 0.08 ± 0.03) does agree well with recent numerical disk galaxy simulations at this mass range (e.g. Crain et al. 2010). In these simulations, most of the gas is in the hot phase, suggesting that the cool baryon content of the most massive spiral galaxies (i.e. considering only stars and cool gas) should be systematically lower than f_b measured in NGC 720.

McGaugh et al. (2010, see also Dai et al. 2009) has assembled $f_{b,500}$ estimates for a sample of massive disk galaxies, *omitting any putative hot halo from the esti-*

mate. Indeed, $f_{b,500}$ in these systems does lie slightly below that in NGC 720. Still, the stellar mass fraction in these spiral galaxies is substantially higher than in NGC 720, and the modest discrepancy in $f_{b,500}$ leaves little room for a massive hot halo around the spirals. This appears inconsistent with the simulations and, at face value, might suggest very different star formation efficiencies between the different types of galaxy. One difficulty with this interpretation, however, is the young (~ 3 Gyr) dominant stellar population in NGC 720, suggesting a recent formation epoch, possibly from a merger event involving massive disk galaxies (Rembold et al. 2005). Since the gas fraction can only be reduced during a merger (as it may be ejected from the galaxy, funnelled onto the central black hole or converted into stars), this implies there must have been at least as much gas as stars within R_{500} in the progenitors. Even allowing for stellar mass loss over the last ~ 3 Gyr, this would require similarly inefficient star formation in the precursor (spiral?) galaxies. We caution that the M_{500} values for the spiral galaxies in McGaugh et al. were obtained by scaling the rotation velocity, rather than formal modelling, which could plausibly introduce some uncertainties into both M_{500} and $f_{b,500}$ reported in that work.

Finally, it is interesting to compare our results to measurements of f_b in the Milky Way, around which there is indirect evidence for an extended, hot halo. This system has M_{vir} in the range $\sim 1\text{--}3 \times 10^{12} M_\odot$ (Klypin et al. 2002; Sakamoto et al. 2003), close to that of NGC 720. Based on the baryonic mass estimate of Flynn et al. (2006), which does not consider any putative hot halo, $f_{b,\text{vir}}$ lies in the range $\sim 0.02\text{--}0.06$. This is suggestively below our measurement for NGC 720 and the discrepancy is most acute towards the more massive end of the Milky Way mass range (i.e. almost the same mass as NGC 720).

6.3. Dark Matter Halo

We have obtained a high-quality measurement of the gravitating mass profile for the isolated elliptical galaxy NGC 720 between $\sim 0.002R_{\text{vir}}$ and $0.2R_{\text{vir}}$ ($\sim 0.7R_{2500}$). As found in past studies of the hot gas around galaxies (e.g. Buote et al. 2002; Humphrey et al. 2006, 2009a; Fukazawa et al. 2006; O’Sullivan et al. 2007; Zhang et al. 2007; Nagino & Matsushita 2009), the data are inconsistent with a constant M/L ratio model. Given the high-quality constraints on the mass profile in NGC 720, this means that dark matter is required at $19.6\text{-}\sigma$.

With these data from deep *Chandra* and *Suzaku* observations, we have been able to obtain unprecedented constraints on the virial mass and dark matter halo concentration at this mass range ($M_{\text{vir}} = 3.1 \pm 0.4 \times 10^{12} M_\odot$). Such a low mass (only a few times more massive than the Milky Way) is consistent with our picture of this system as an isolated elliptical galaxy, rather than a galaxy group *per se*. These results are in agreement with, but very much tighter than, those found by Humphrey et al. (2006) for the same system. This improvement partially reflects the much better data used here (~ 100 ks of *Chandra* data, plus ~ 180 ks of *Suzaku* time, as compared to the ~ 17 ks *Chandra* dataset used by Humphrey et al.), but is also on account of various refinements made to our mass modelling procedure in the interim. Of particular significance is the adoption of parametrized models for the entropy (rather than the temperature) distribution,

allowing us to enforce a monotonically rising entropy profile (i.e. the Schwarzschild criterion for stability against convection). This efficiently eliminates unphysical portions of parameter space. Similarly, explicitly requiring the gas to remain approximately hydrostatic out to the virial radius also restricts parameter space to regions containing only physical models, whereas the fitting procedure of H06 was less restrictive.

In large part, the tight constraints on the virial mass and concentration are due to the ability of the data to constrain the flattening of the mass profile outside ~ 20 kpc. This scale is much larger than the effective radius of the galaxy (3.1 kpc), and is thus unrelated to the stellar-dark matter conspiracy (Humphrey & Buote 2010), and instead must indicate the scale radius of the dark matter halo. As discussed in Gastaldello et al. (2007b), the ability to constrain the virial quantities is very sensitive to the accurate measurement of the scale radius. This flattening is not model dependent; when fitting the “cored logarithmic” DM model, we similarly found a flattening in the total gravitating mass profile at this scale²¹.

The small DM scale radius in NGC 720 indicates a high concentration; indeed, we find that it lies ~ 3 times the intrinsic scatter above the predicted median relation found in dark matter only simulations for the “ Λ CDM1” (“concordance”) cosmology by Macciò et al. (2008). Buote et al. (2007) measured the $c\text{--}M_{\text{vir}}$ relation empirically for a sample of early-type galaxies, groups and clusters, finding higher concentrations in the galaxy regime ($\lesssim 10^{13} M_\odot$) than Macciò et al. Still, we find that NGC 720 lies ~ 2 times the intrinsic scatter above this relation²². The extreme isolation of NGC 720 suggests an early epoch of formation (such that the brightest subhalos have merged to form the central object), which should give rise to a higher DM halo concentration, and may provide a possible explanation for the measured c_{vir} (e.g. Zentner et al. 2005). The very young (~ 3 Gyr) mean age for the central stellar population may simply reflect stars formed in a recent gas-rich merger rather than a realistic estimate of the age of the population as a whole (see discussion in § 6.1).

One factor which could lead to an over-estimate of c_{vir} is a failure to model correctly the stellar mass component (Mamon & Lokas 2005; Humphrey et al. 2006). If the young stellar population which dominates the light is, indeed, only a fraction of the total population in the galaxy, it is plausible that the assumption that mass follows light is not correct (although the modest colour gradient of the galaxy is not consistent with a dramatic violation of this assumption: Peletier et al. 1990). However, excluding

²¹ We note that the best-fitting mass profile agrees with that reported by Humphrey & Buote (2010), who found that, within ~ 30 kpc, it is approximately consistent with a powerlaw. In that case, the data lacked the radial coverage to constrain the subtle flattening between $\sim 20\text{--}30$ kpc, within which there is only a single data bin. Furthermore, the slope of the mass profile was insensitive to the exact radial fitting range adopted, so our conclusions in Humphrey & Buote (2010) are not affected by our failure to correct for this flattening.

²² Strictly speaking, this comparison is not independent, since NGC 720 was one of the systems used to determine the Buote et al. (2007) relation, albeit with much poorer data. Nevertheless, NGC 720 does not appear to be unusual in comparison to the other systems used by these authors, and so it is unlikely that this relation is largely driven by this one data-point.

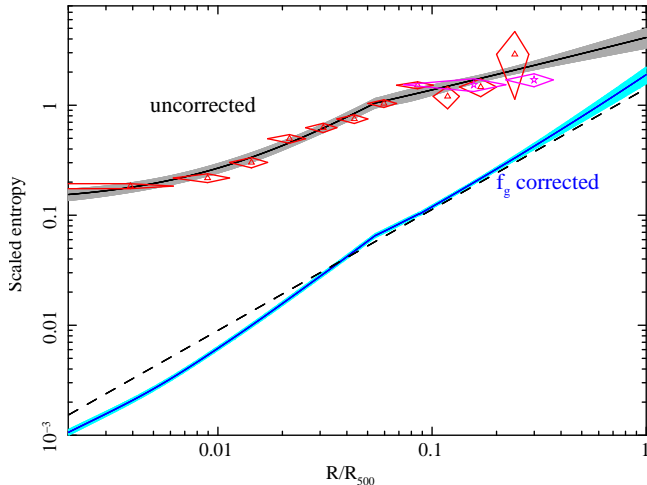


FIG. 12.— $1\text{-}\sigma$ confidence region for the entropy profile model of NGC 720, scaled by its characteristic entropy K_{500} ($=27.9$ keV cm^2), and shown as a function of R_{500} . We overlay the deprojected entropy data-points (shown in Fig 5), similarly scaled. The dotted line indicates the “baseline” prediction from gravitational structure formation (Voit et al. 2005). Also shown is the scaled entropy model, corrected for the gas fraction profile (“ f_g corrected”; see text), which agrees very well with the baseline model.

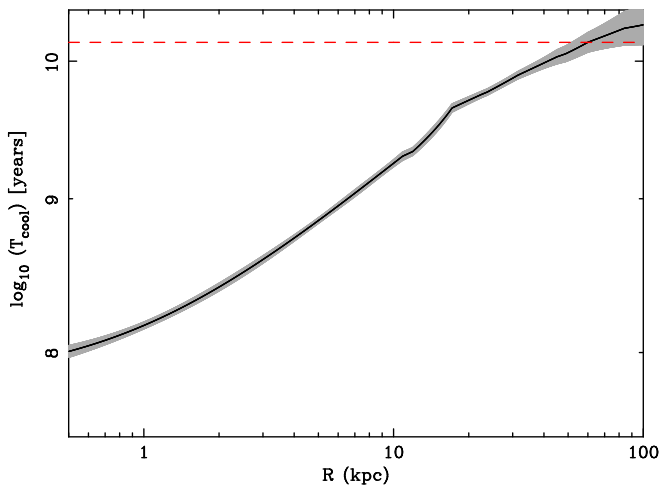


FIG. 13.— Cooling time of the gas (solid line), and its $1\text{-}\sigma$ confidence region (shaded region). Error bars do not incorporate abundance errors (which are less than $\sim 20\%$). Gas inside ~ 60 kpc has a cooling time shorter than the Hubble Time (shown as a dashed line).

the central ~ 4 kpc ($\sim 1.3R_e$) does not significantly affect the concentration (§ 5.8). Alternatively, if adiabatic contraction operates, it should increase the cuspsness of the central DM halo profile, for a fixed stellar M/L ratio, which could also lead to c_{vir} being over-estimated if it is not accounted for (e.g. Napolitano et al. 2010). Fitting an AC model (§ 5.1) also led to a slightly less concentrated halo, but the effect was not large enough to reconcile the best-fitting value with the Macciò et al. (2008) predictions. This comparative lack of sensitivity of the concentration to the details of the stellar modelling is not altogether surprising, since R_e (3.1 kpc) is far smaller than the scale radius of the DM halo.

6.4. Entropy profile

As expected for gas which is approximately hydrostatic, we obtain a good fit to the temperature and density profiles with a monotonically rising entropy profile. Although the entropy profile slope in the inner part of the system (β_1) is close to the canonical 1.1 (Table 2) predicted by gravitational structure formation simulations (considering only gravity without cooling or feedback: Voit et al. 2005), the profile flattens at smaller and larger radii. This is consistent with two of the three galaxies studied in Humphrey et al. (2009a), and similarly shaped profiles have also been observed in galaxy groups (e.g. Jetha et al. 2007; Finoguenov et al. 2007; Gastaldello et al. 2007a; Sun et al. 2009; Flohic et al. 2010).

In Fig 12 we show the entropy profile as a function of R_{500} , and scaled by the “characteristic entropy”, K_{500} (e.g. Pratt et al. 2010). Clearly the profile is significantly flatter than the “baseline” model predicted by gravity-only simulations (Voit et al. 2005), and the normalization is significantly enhanced, reflecting the injection of entropy by non-gravitational processes, especially in the inner regions. In comparison with galaxy groups and clusters (e.g. Pratt et al. 2010; Sun et al. 2009), the entropy profile is more discrepant with the baseline model, reflecting the greater impact of nongravitational heating on a lower mass halo. Nevertheless, the entropy injection still appears insufficient to evacuate a significant fraction of the baryons from the halo, as indicated by the approximate baryonic closure within R_{vir} . While this may reflect a finely-balanced heating mechanism in the system, we note that most of the gas lies at large radii, where the entropy profiles are much less discrepant (for example, $\sim 65\%$ of the gas lies outside R_{500}).

If nongravitational processes primarily redistribute the gas, rather than raising its temperature, we might expect the entropy profile to be simply related to the baseline model and the gas mass profile. Indeed Pratt et al. (2010) demonstrated with their cluster sample that the product $S(R) (f_g(R)/f_{b,U})^{2/3}$, where S is the entropy profile, $f_g(R)$ is the gas mass fraction profile (Fig 9) and $f_{b,U}$ is the Universal baryon fraction (0.17), is very close to the baseline model. It is interesting to investigate whether this also holds for lower-mass halos, where the impact of nongravitational heating is systematically larger. We show the “ f_g corrected” entropy profile for NGC 720 in Fig 12, finding that it also lies very close the gravity-only predictions, even in a \sim Milky Way-mass halo. We note that the corrected entropy profile agrees with this relation even when extrapolated outside the projected radii at which there are data, which provides support for our extrapolated entropy profile.

In order to interpret the impact of non-gravitational processes on the entropy distribution, it is helpful to consider the cooling time of the gas. In Fig 13, we show that, within ~ 60 kpc, it is shorter than the Hubble time. Nevertheless, only $\sim 6\%$ of the gas is currently within this region, implying that most of the gas in NGC 720 will not have had sufficient time to cool. In part this reflects the significant non-gravitational heating that has raised the entropy even in these outer regions significantly above the baseline model (Fig 12). The average stellar age in NGC 720 is young (~ 3 Gyr), and if this reflects the time since NGC 720 formed, only the gas within ~ 15 kpc would have had time to cool, within which there

is presently only $\sim 0.5\%$ ($\sim 10^9 M_\odot$) of the total gas mass.

6.5. Abundance gradient

One of the intriguing results from our study is the detection, with both *Chandra* and *Suzaku*, of a strong negative abundance gradient in the hot gas of NGC 720 (Fig 3), making it arguably the lowest-mass system in which such a gradient has been definitively detected. Although the metallicity of the ISM in early-type galaxies with intermediate to high X-ray luminosities is now known to be \sim Solar, and comparable to the stellar metallicity (Humphrey & Buote 2006; Ji et al. 2009), simple chemical enrichment models typically predict substantially more metals in the central part of the halo, where enrichment from supernovae and stellar mass-loss is concentrated (e.g. Pipino et al. 2005). Solutions to this problem may involve large-scale mixing due to AGN-ISM interaction, or the assembly of structure through mergers (Mathews et al. 2004; Cora 2006; Cox et al. 2006). Clearly the spatial distribution of the metals in the hot gas is a useful constraint on any model predicting large-scale mixing.

While, to date, very little is known about the radial dependence of Z_{Fe} in the ISM of galaxy-scale halos, recent *Chandra* and *XMM* studies of relaxed galaxy groups have revealed similar, centrally peaked Z_{Fe} profiles (e.g. Humphrey & Buote 2006; Buote 2002; Buote et al. 2003; Rasmussen & Ponman 2007). Mathews et al. (2004) were able to explain the overall shape of these group-scale profiles by invoking large-scale flows driven by low-level AGN heating. It remains to be seen whether such a model could also explain the observed abundance profile of NGC 720 which, residing in a much shallower potential well, should be more susceptible to the effects of feedback.

7. CONCLUSIONS

Based on an analysis of data from deep new *Chandra* and *Suzaku* observations, we have obtained unprecedented constraints on the temperature, density and heavy metal abundance in the hot gas halo of the \sim Milky Way-mass isolated elliptical galaxy NGC 720. This has allowed us to measure in fine detail both the total gravitating mass distribution and the baryon fraction out to large scales. In summary:

1. The relaxed X-ray morphology of NGC 720, lack of radio emission, and the good fits obtained from our hydrostatic models to the nontrivial temperature and density profile indicate that the gas must be close to hydrostatic.
2. A constant M/L ratio model for the gravitating mass distribution is ruled out in favour of a model including an NFW dark matter halo at high significance ($\sim 20\text{-}\sigma$).
3. Assuming an NFW dark matter halo, we obtained unprecedented, tight constraints on both the virial mass and concentration for such a low-mass system

($M_{2500} = 1.6 \pm 0.2 \times 10^{12} M_\odot$ with systematic errors typically $\lesssim 20\%$; $M_{\text{vir}} = 3.1^{+0.4}_{-0.3} \times 10^{12} M_\odot$). This confirms that an isolated elliptical galaxy that is not at the centre of a massive group can maintain a substantial dark matter halo.

4. The total gas mass inferred within R_{vir} substantially exceeds the stellar mass, with most of the gas lying outside ~ 100 kpc. This supports theoretical predictions that Milky Way-mass galaxies can host massive, quasi-hydrostatic hot gas halos. It remains to be seen if less isolated galaxies can, similarly, maintain such a halo.

5. Self-consistently extrapolated to R_{vir} , the baryon fraction is consistent with the Cosmological value (0.17), indicating that it is possible even for a \sim Milky Way-mass galaxy to be baryonically closed, at least if (relatively) isolated.

6. Within both R_{2500} and R_{500} , the gas fraction (and the baryon fraction in the case of R_{500}) of NGC 720 are both consistent with an extrapolation to low masses of the trends seen for groups and clusters.

7 After correcting for the gas fraction, the entropy profile is close to the self-similar predictions of gravitational structure formation simulations, as observed in massive galaxy clusters.

8. Both the *Chandra* and *Suzaku* data reveal evidence of a strong heavy metal abundance gradient, qualitatively similar to those observed in relaxed, massive galaxy groups and clusters.

We would like to thank Taotao Fang for insightful and helpful discussions. We also benefitted greatly from discussions with H el ene Flohic, Erik Tollerud, James Bullock and Pepi Fabbiano. This research has made use of data obtained from the High Energy Astrophysics Science Archive Research Center (HEASARC), provided by NASA's Goddard Space Flight Center. This research has also made use of the NASA/IPAC Extragalactic Database (*NED*) which is operated by the Jet Propulsion Laboratory, California Institute of Technology, under contract with NASA, and the HyperLEDA database (<http://leda.univ-lyon1.fr>). We are grateful to the ACE/SWEPAM instrument team for making their data publicly available through the ACE Science Center. PJH and DAB gratefully acknowledge partial support from NASA under Grant NNX10AD07G, issued through the office of Space Science Astrophysics Data Program. Partial support for this work was also provided by NASA under Grant NNG04GE76G issued through the Office of Space Sciences Long-Term Space Astrophysics Program, and by *Chandra* awards GO6-7071X and GO9-0092X, issued by the Chandra X-Ray Center, which is operated by the Smithsonian Astrophysical Observatory for and on behalf of NASA. We are also grateful for partial support from NASA-*Suzaku* grants NNX09AC71G and NNX10AH85G and NASA-*XMM* grant NNX08AX74G.

REFERENCES

- Abadi, M. G., Navarro, J. F., Fardal, M., Babul, A., & Steinmetz, M. 2009, arXiv:0902.2477
- Allen, S. W., Rapetti, D. A., Schmidt, R. W., Ebeling, H., Morris, R. G., & Fabian, A. C. 2008, *MNRAS*, 383, 879
- Anderson, M. E. & Bregman, J. N. 2010, *ApJ*, 714, 320
- Asplund, M., Grevesse, N., & Sauval, J. 2004, in *Cosmic abundances as records of stellar evolution and nucleosynthesis*, ed. F. N. Bash & T. G. Barnes (ASP Conf. series), astro-ph/0410214

- Benson, A. J., Bower, R. G., Frenk, C. S., Lacey, C. G., Baugh, C. M., & Cole, S. 2003, *ApJ*, 599, 38
- Benson, A. J., Bower, R. G., Frenk, C. S., & White, S. D. M. 2000, *MNRAS*, 314, 557
- Binney, J. & Tremaine, S. 2008, *Galactic Dynamics* (2nd ed.; Princeton, NJ: Princeton University Press)
- Binney, J. J., Davies, R. L., & Illingworth, G. D. 1990, *ApJ*, 361, 78
- Blitz, L. & Robishaw, T. 2000, *ApJ*, 541, 675
- Blumenthal, G. R., Faber, S. M., Flores, R., & Primack, J. R. 1986, *ApJ*, 301, 27
- Bregman, J. N. & Lloyd-Davies, E. J. 2007, *ApJ*, 669, 990
- Brighenti, F., Mathews, W. G., Humphrey, P. J., & Buote, D. A. 2009, *ApJ*, 705, 1672
- Brough, S., Forbes, D. A., Kilborn, V. A., & Couch, W. 2006, *MNRAS*, 370, 1223
- Bryan, G. L. & Norman, M. L. 1998, *ApJ*, 495, 80
- Buote, D. A. 2000, *MNRAS*, 311, 176
- Buote, D. A. 2002, *ApJ*, 574, L135
- Buote, D. A. & Canizares, C. R. 1994, *ApJ*, 427, 86
- Buote, D. A. & Canizares, C. R. 1996, *ApJ*, 468, 184
- Buote, D. A., Gastaldello, F., Humphrey, P. J., Zappacosta, L., Bullock, J. S., Brighenti, F., & Mathews, W. G. 2007, *ApJ*, 664, 123
- Buote, D. A. & Humphrey, P. J. 2010, in preparation
- Buote, D. A., Jeltema, T. E., Canizares, C. R., & Garmire, G. P. 2002, *ApJ*, 577, 183
- Buote, D. A., Lewis, A. D., Brighenti, F., & Mathews, W. G. 2003, *ApJ*, 595, 151
- Buote, D. A. & Tsai, J. C. 1995, *ApJ*, 439, 29
- Buote, D. A., Zappacosta, L., Fang, T., Humphrey, P. J., Gastaldello, F., & Tagliaferri, G. 2009, *ApJ*, 695, 1351
- Canizares, C. R., Fabbiano, G., & Trinchieri, G. 1987, *ApJ*, 312, 503
- Cash, W. 1976, *A&A*, 52, 307
- Cash, W. 1979, *ApJ*, 228, 939
- Churazov, E., Forman, W., Vikhlinin, A., Tremaine, S., Gerhard, O., & Jones, C. 2008, *MNRAS*, 388, 1062
- Cora, S. A. 2006, *MNRAS*, 368, 1540
- Cox, T. J., Di Matteo, T., Hernquist, L., Hopkins, P. F., Robertson, B., & Springel, V. 2006, *ApJ*, 643, 692
- Crain, R. A., McCarthy, I. G., Frenk, C. S., Theuns, T., & Schaye, J. 2010, *MNRAS*, in press (arXiv:1005.1642)
- Dai, X., Bregman, J. N., Kochanek, C. S., & Rasia, E. 2009, *ApJ*, submitted (arXiv:0911.2230)
- Dai, X., Kochanek, C. S., & Morgan, N. D. 2007, *ApJ*, 658, 917
- David, L. P., Jones, C., Forman, W., Vargas, I. M., & Nulsen, P. 2006, *ApJ*, 653, 207
- Davis, J. E. 2001, *ApJ*, 548, 1010
- de Vaucouleurs, G., de Vaucouleurs, A., Corwin, H. G., Buta, R. J., Paturel, G., & Fouque, P. 1991, *Third Reference Catalogue of Bright Galaxies* (Volume 1-3, XII, 2069 pp. 7 figs.. Springer-Verlag Berlin Heidelberg New York)
- Dickey, J. M. & Lockman, F. J. 1990, *ARA&A*, 28, 215
- Diehl, S. & Statler, T. S. 2007, *ApJ*, 668, 150
- Dressler, A., Schechter, P. L., & Rose, J. A. 1986, *AJ*, 91, 1058
- Dunkley, J., et al. 2009, *ApJS*, 180, 306
- Ellis, S. C. & O'Sullivan, E. 2006, *MNRAS*, 367, 627
- Fabbiano, G., Klein, U., Trinchieri, G., & Wielebinski, R. 1987, *ApJ*, 312, 111
- Fabbiano, G., Zezas, A., & Murray, S. S. 2001, *ApJ*, 554, 1035
- Fang, T., Buote, D. A., Humphrey, P. J., Canizares, C. R., Zappacosta, L., Maiolino, R., Tagliaferri, G., & Gastaldello, F. 2010, *ApJ*, 714, 1715
- Fang, T., Humphrey, P., & Buote, D. 2009, *ApJ*, 691, 1648
- Fang, T., Marshall, H. L., Lee, J. C., Davis, D. S., & Canizares, C. R. 2002, *ApJ*, 572, L127
- Fang, T., Mckee, C. F., Canizares, C. R., & Wolfire, M. 2006, *ApJ*, 644, 174
- Feroz, F. & Hobson, M. P. 2008, *MNRAS*, 384, 449
- Feroz, F., Hobson, M. P., & Bridges, M. 2009, *MNRAS*, 398, 1601
- Finoguenov, A. & Jones, C. 2001, *ApJ*, 547, L107
- Finoguenov, A., Ponman, T. J., Osmond, J. P. F., & Zimer, M. 2007, *MNRAS*, 374, 737
- Flohic, H. M. L. G. et al. 2010, in preparation
- Flynn, C., Holmberg, J., Portinari, L., Fuchs, B., & Jahreiß, H. 2006, *MNRAS*, 372, 1149
- Forman, W., et al. 2007, *ApJ*, 665, 1057
- Fukazawa, Y., Botoya-Nonesca, J. G., Pu, J., Ohto, A., & Kawano, N. 2006, *ApJ*, 636, 698
- Fukugita, M., Hogan, C. J., & Peebles, P. J. E. 1998, *ApJ*, 503, 518
- Fukugita, M. & Peebles, P. J. E. 2006, *ApJ*, 639, 590
- Garcia, A. M. 1993, *A&AS*, 100, 47
- Gastaldello, F., Buote, D. A., Humphrey, P. J., Zappacosta, L., Brighenti, F., & Mathews, W. G. 2007a, in *Heating versus Cooling in Galaxies and Clusters of Galaxies*, ed. H. Böhringer, G. W. Pratt, A. Finoguenov, & P. Schuecker, 275
- Gastaldello, F., Buote, D. A., Humphrey, P. J., Zappacosta, L., Bullock, J. S., Brighenti, F., & Mathews, W. G. 2007b, *ApJ*, 669, 158
- Gavazzi, R. 2005, *A&A*, 443, 793
- Gavazzi, R., Treu, T., Rhodes, J. D., Koopmans, L. V. E., Bolton, A. S., Burles, S., Massey, R. J., & Moustakas, L. A. 2007, *ApJ*, 667, 176
- Gebhardt, K., Richstone, D., Ajhar, E. A., Lauer, T. R., Byun, Y.-I., Kormendy, J., Dressler, A., Faber, S. M., Grillmair, C., & Tremaine, S. 1996, *AJ*, 112, 105
- Gebhardt, K. & Thomas, J. 2009, *ApJ*, 700, 1690
- Giodini, S., et al. 2009, *ApJ*, 703, 982
- Gnedin, O. Y., Kravtsov, A. V., Klypin, A. A., & Nagai, D. 2004, *ApJ*, 616, 16
- Gnedin, O. Y., Weinberg, D. H., Pizagno, J., Prada, F., & Rix, H.-W. 2007, *ApJ*, 671, 1115
- Gould, A. 2003, preprint, astro-ph/0310577
- Henley, D. B., Shelton, R. L., Kwak, K., Young, M. R., & Mac Low, M.-M. 2010, *ApJ*, submitted, astro-ph/1005.1085
- Hoekstra, H., Hsieh, B. C., Yee, H. K. C., Lin, H., & Gladders, M. D. 2005, *ApJ*, 635, 73
- Huchtmeier, W. K. 1994, *A&A*, 286, 389
- Humphrey, P. J. & Buote, D. A. 2006, *ApJ*, 639, 136
- Humphrey, P. J. & Buote, D. A. 2008, *ApJ*, 689, 983
- Humphrey, P. J. & Buote, D. A. 2010, *MNRAS*, 403, 2143
- Humphrey, P. J., Buote, D. A., Brighenti, F., Gebhardt, K., & Mathews, W. G. 2008, *ApJ*, 683, 161
- Humphrey, P. J., Buote, D. A., Brighenti, F., Gebhardt, K., & Mathews, W. G. 2009a, *ApJ*, 703, 1257, (H09)
- Humphrey, P. J., Buote, D. A., Gastaldello, F., Zappacosta, L., Bullock, J. S., Brighenti, F., & Mathews, W. G. 2006, *ApJ*, 646, 899, (H06)
- Humphrey, P. J., Liu, W., & Buote, D. A. 2009b, *ApJ*, 693, 822
- Ishisaki, Y., et al. 2007, *PASJ*, 59, 113
- Jetha, N. N., Ponman, T. J., Hardcastle, M. J., & Croston, J. H. 2007, *MNRAS*, 376, 193
- Ji, J., Irwin, J. A., Athey, A., Bregman, J. N., & Lloyd-Davies, E. J. 2009, *ApJ*, 696, 2252
- Jones, C., Forman, W., Vikhlinin, A., Markevitch, M., David, L., Warmflash, A., Murray, S., & Nulsen, P. E. J. 2002, *ApJ*, 567, L115
- Joudaki, S., Smidt, J., Amblard, A., & Cooray, A. 2010, *ApJ*, submitted (arXiv:1002.4872)
- Kauffmann, G., Colberg, J. M., Diaferio, A., & White, S. D. M. 1999, *MNRAS*, 303, 188
- Kereš, D., Katz, N., Weinberg, D. H., & Davé, R. 2005, *MNRAS*, 363, 2
- Kilborn, V. A., Forbes, D. A., Barnes, D. G., Koribalski, B. S., Brough, S., & Kern, K. 2009, *MNRAS*, 400, 1962
- Kim, D. & Fabbiano, G. 2004, *ApJ*, 613, 933
- Klypin, A., Zhao, H., & Somerville, R. S. 2002, *ApJ*, 573, 597
- Koopmans, L. V. E., Bolton, A., Treu, T., Czoske, O., Auger, M. W., Barnabè, M., Vegetti, S., Gavazzi, R., Moustakas, L. A., & Burles, S. 2009, *ApJ*, 703, L51
- Kriss, G. A., Cioffi, D. F., & Canizares, C. R. 1983, *ApJ*, 272, 439
- Kroupa, P. 2001, *MNRAS*, 322, 231
- Lewis, A. D., Buote, D. A., & Stocke, J. T. 2003, *ApJ*, 586, 135
- Lucy, L. B. 1974, *AJ*, 79, 745
- Macciò, A. V., Dutton, A. A., & van den Bosch, F. C. 2008, *MNRAS*, 391, 1940
- Mahdavi, A., Hoekstra, H., Babul, A., & Henry, J. P. 2008, *MNRAS*, 384, 1567
- Maller, A. H. & Bullock, J. S. 2004, *MNRAS*, 355, 694
- Mamon, G. A. & Lokas, E. L. 2005, *MNRAS*, 362, 95
- Mathews, W. G., Brighenti, F., & Buote, D. A. 2004, *ApJ*, 615, 662

- Mathews, W. G., Brighenti, F., Faltenbacher, A., Buote, D. A., Humphrey, P. J., Gastaldello, F., & Zappacosta, L. 2006, *ApJ*, 652, L17
- Mathews, W. G., Faltenbacher, A., Brighenti, F., & Buote, D. A. 2005, *ApJ*, 634, L137
- Mazzotta, P., Rasia, E., Moscardini, L., & Tormen, G. 2004, *MNRAS*, 354, 10
- McCarthy, I. G., Schaye, J., Ponman, T. J., Bower, R. G., Booth, C. M., Dalla Vecchia, C., Crain, R. A., Springel, V., Theuns, T., & Wiersma, R. P. C. 2010, *MNRAS*, in press (arXiv:0911.2641)
- McComas, D. J., Bame, S. J., Barker, P., Feldman, W. C., Phillips, J. L., Riley, P., & Griffee, J. W. 1998, *Space Science Reviews*, 86, 563
- McGaugh, S. S., Schombert, J. M., de Blok, W. J. G., & Zagursky, M. J. 2010, *ApJ*, 708, L14
- Million, E. T., Werner, N., Simionescu, A., Allen, S. W., Nulsen, P. E. J., Fabian, A. C., Böhringer, H., & Sanders, J. S. 2010, *MNRAS* in press (arXiv:1006.5484)
- Moore, B. & Davis, M. 1994, *MNRAS*, 270, 209
- Nagai, D., Vikhlinin, A., & Kravtsov, A. V. 2007, *ApJ*, 655, 98
- Nagino, R. & Matsushita, K. 2009, *A&A*, 501, 157
- Napolitano, N. R., Romanowsky, A. J., & Tortora, C. 2010, *MNRAS*, in press
- Navarro, J. F., Frenk, C. S., & White, S. D. M. 1997, *ApJ*, 490, 493
- Nicastro, F., Zezas, A., Drake, J., Elvis, M., Fiore, F., Fruscione, A., Marengo, M., Mathur, S., & Bianchi, S. 2002, *ApJ*, 573, 157
- Osmond, J. P. F. & Ponman, T. J. 2004, *MNRAS*, 350, 1511
- O'Sullivan, E., Forbes, D. A., & Ponman, T. J. 2001, *MNRAS*, 328, 461
- O'Sullivan, E., Vrtilik, J. M., Harris, D. E., & Ponman, T. J. 2007, *ApJ*, 658, 299
- Peletier, R. F., Davies, R. L., Illingworth, G. D., Davis, L. E., & Cawson, M. 1990, *AJ*, 100, 1091
- Piffaretti, R., Jetzer, P., & Schindler, S. 2003, *A&A*, 398, 41
- Piffaretti, R. & Valdarnini, R. 2008, *A&A*, 491, 71
- Pipino, A., Kawata, D., Gibson, B. K., & Matteucci, F. 2005, *A&A*, 434, 553
- Pointecouteau, E., Arnaud, M., & Pratt, G. W. 2005, *A&A*, 435, 1
- Ponman, T. J., Cannon, D. B., & Navarro, J. F. 1999, *Nature*, 397, 135
- Pratt, G. W., Arnaud, M., Piffaretti, R., Böhringer, H., Ponman, T. J., Croston, J. H., Voit, G. M., Borgani, S., & Bower, R. G. 2010, *A&A*, 511, A85
- Pratt, G. W., Croston, J. H., Arnaud, M., & Böhringer, H. 2009, *A&A*, 498, 361
- Protassov, R., van Dyk, D. A., Connors, A., Kashyap, V. L., & Siemiginowska, A. 2002, *ApJ*, 571, 545
- Purcell, C. W., Bullock, J. S., & Zentner, A. R. 2007, *ApJ*, 666, 20
- Rasmussen, A., Kahn, S. M., & Paerels, F. 2003, in *Astrophysics and Space Science Library*, Vol. 281, *The IGM/Galaxy Connection. The Distribution of Baryons at z=0*, ed. J. L. Rosenberg & M. E. Putman, 109–+
- Rasmussen, J. & Ponman, T. J. 2007, *MNRAS*, 380, 1554
- Rasmussen, J., Sommer-Larsen, J., Pedersen, K., Toft, S., Benson, A., Bower, R. G., & Grove, L. F. 2009, *ApJ*, 697, 79
- Rembold, S. B., Pastoriza, M. G., & Bruzual, G. 2005, *A&A*, 436, 57
- Revnivtsev, M., Churazov, E., Sazonov, S., Forman, W., & Jones, C. 2008, *A&A*, 490, 37
- Romanowsky, A. J., Strader, J., Spitler, L. R., Johnson, R., Brodie, J. P., Forbes, D. A., & Ponman, T. 2009, *AJ*, 137, 4956
- Sakamoto, T., Chiba, M., & Beers, T. C. 2003, *A&A*, 397, 899
- Sembach, K. R., Wakker, B. P., Savage, B. D., Richter, P., Meade, M., Shull, J. M., Jenkins, E. B., Sonneborn, G., & Moos, H. W. 2003, *ApJS*, 146, 165
- Sengupta, C., Balasubramanyam, R., & Dwarakanath, K. S. 2007, *MNRAS*, 378, 137
- Shen, J. & Gebhardt, K. 2010, *ApJ*, 711, 484
- Snowden, S. L., Collier, M. R., & Kuntz, K. D. 2004, *ApJ*, 610, 1182
- Sommer-Larsen, J. 2006, *ApJ*, 644, L1
- Sommer-Larsen, J., Götz, M., & Portinari, L. 2003, *ApJ*, 596, 47
- Strickland, D. K., Heckman, T. M., Colbert, E. J. M., Hoopes, C. G., & Weaver, K. A. 2004, *ApJS*, 151, 193
- Sun, M., Voit, G. M., Donahue, M., Jones, C., Forman, W., & Vikhlinin, A. 2009, *ApJ*, 693, 1142
- Tawara, Y., Matsumoto, C., Tozuka, M., Fukazawa, Y., Matsushita, K., & Anabuki, N. 2008, *PASJ*, 60, 307
- Thomas, J., Jesseit, R., Naab, T., Saglia, R. P., Burkert, A., & Bender, R. 2007a, *MNRAS*, 381, 1672
- Thomas, J., Saglia, R. P., Bender, R., Thomas, D., Gebhardt, K., Magorrian, J., Corsini, E. M., & Wegner, G. 2007b, *MNRAS*, 382, 657
- Tollerud, E. J., Bullock, J. S., Strigari, L. E., & Willman, B. 2008, *ApJ*, 688, 277
- Tonry, J. L., Dressler, A., Blakeslee, J. P., Ajhar, E. A., Fletcher, A., Luppino, G. A., Metzger, M. R., & Moore, C. B. 2001, *ApJ*, 546, 681
- Tremaine, S., et al. 2002, *ApJ*, 574, 740
- Tsai, J. C., Katz, N., & Bertschinger, E. 1994, *ApJ*, 423, 553
- Vikhlinin, A., Kravtsov, A., Forman, W., Jones, C., Markevitch, M., Murray, S. S., & Van Speybroeck, L. 2006, *ApJ*, 640, 691
- Voit, G. M., Kay, S. T., & Bryan, G. L. 2005, *MNRAS*, 364, 909
- Welch, G. A., Sage, L. J., & Young, L. M. 2010, *ApJ*, in press (arXiv:1009.5259)
- White, S. D. M. & Frenk, C. S. 1991, *ApJ*, 379, 52
- Yao, Y., Nowak, M. A., Wang, Q. D., Schulz, N. S., & Canizares, C. R. 2008, *ApJ*, 672, L21
- Yao, Y. & Wang, Q. D. 2005, *ApJ*, 624, 751
- Zappacosta, L., Buote, D. A., Gastaldello, F., Humphrey, P. J., Bullock, J., Brighenti, F., & Mathews, W. 2006, *ApJ*, 650, 777
- Zentner, A. R., Berlind, A. A., Bullock, J. S., Kravtsov, A. V., & Wechsler, R. H. 2005, *ApJ*, 624, 505
- Zhang, Z., Xu, H., Wang, Y., An, T., Xu, Y., & Wu, X. 2007, *ApJ*, 656, 805